Chapter 7
Airfoil Aerodynamics

Abstract In this chapter we present the aerodynamics about two-dimensional lift-producing wing sections (airfoils) at low transonic conditions. It is shown how various design parameters influence the velocity distribution and the shock formation over an airfoil. The development of supercritical airfoils is explained from a historic perspective. First the advantages of natural laminar flow sections are explained for subsonic conditions prior to the formation local supersonic flow. It is shown how the supercritical airfoil distinguishes itself in terms pressure distribution and drag behavior once transonic conditions are encountered. Furthermore, it is demonstrated that transonic flow limitations can play a major role in the maximum lift coefficient of (multi-element) airfoils at Mach numbers as low as 0.25. A theoretical limit of the local Mach number is derived that effectively limits the amount of suction that can be generated over the upper surface of an airfoil. Also the concept of shock-boundary layer interaction is further expanded in this chapter. It is shown how periodic separation at the shock foot and shock oscillation can interact to produce a high-frequency pressure fluctuation known as transonic buffet. This chapter contains 4 examples and 16 practice problems at the end of the chapter.

7.1 Introduction

Experimental research into transonic aerodynamics was initiated before the first world war. Although initially tailored towards munition, at the end of WWI transonic effects were showing up in the increased tip speeds of propellers. It was found that thicker sections at the tip yielded much less thrust and a much higher drag coefficient. Soon it was found that when these sections were made thinner, these adverse effects were not encountered [2]. Even though the physical understanding of transonic aerodynamics was still non-existing at the time, practical solutions to the adverse effects were already conceived. Experimental research in transonic aerodynamics always prevailed above the theoretical research because of the many challenges associated with modeling of transonic flow.

With the introduction of the jet engine on transport aircraft in 1949 on the de Havilland Comet, the operating Mach numbers for passenger aircraft increased

R. Vos and S. Farokhi, *Introduction to Transonic Aerodynamics*,
Fluid Mechanics and Its Applications 110, DOI 10.1007/978-94-017-9747-4_7

substantially. It was soon found that the profile shapes of the popular natural-laminar flow airfoils produced significant wave drag and were therefore not suitable for this new type of aircraft. The application of such airfoils required relatively large sweep angles in order to increase the Mach number at which strong shock waves started to cause excessive wave drag. Even though the swept wing solution worked well from a cruise-performance point of view, it posed drawbacks in the low-speed regime as well as in weight and aeroelastic performance. Better airfoil sections were therefore pivotal in the development of contemporary wings on high-subsonic aircraft.

We have seen in Chap. 6 that any body submersed in a flow field produces a pressure distribution. When the integral of the pressure distribution over the entire body is nonzero, a resultant force is produced. We showed that for nonlifting bodies this resulting force is comprised only of the drag force. Such conditions only apply for (axis) symmetric bodies at zero angle of attack. Whenever either of these requirements is violated a resultant force component perpendicular to the freestream direction results. This discrete force (often referred to as the lift) has a point of application somewhere on the body. The resultant force is now a combination of the lift force and the drag force, as shown in Fig. 6.1. When this body is two-dimensional it reduces to an airfoil. For many high-aspect ratio wings, the flow over the center section of the wing can be treated as two-dimensional. Airfoil shape therefore plays an important role in the lift and drag characteristics of the wing.

This chapter explains the typical transonic flow characteristics about two-dimensional airfoil sections (commonly referred to as *airfoils*). We use a historical approach to take the reader on a quest to discover the relevant aerodynamic effects related to transonic flow about airfoils. We demonstrate how experimental researchers such as Pearcey and Whitcomb in the late 1940s and early 1950s came up with airfoils designed for supercritical conditions. They showed how sections could be shaped to operate at high Mach numbers and at high lift coefficients without a large (wave) drag penalty. We present the key differences between laminar-flow airfoils and supercritical airfoils. We also discover that transonic flow about airfoils is not limited to high-subsonic freestream Mach numbers. On the contrary, the maximum lift coefficient is shown to be highly dependent on the freestream Mach number. Especially multi-element airfoils are shown to yield lower maximum lift coefficients due to transonic effects at Mach numbers as low as 0.2. Finally, we present the concept of transonic buffeting: a high-frequency, self-sustained oscillation of the shock wave that severely limits the maximum lift coefficient of an airplane at its operating Mach number and beyond.

7.2 Pressure Distribution About Airfoils

The pressure distribution about airfoils can be understood by following the same rationale as in Sect. 6.2. Concave curvatures on a body cause a deceleration of the flow, which are accompanied by an increase in static pressure. Convex curvatures accelerate the flow and result in a decrease in static pressure (suction). The magnitude

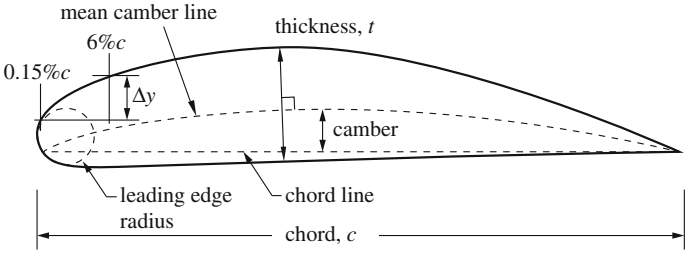

Fig. 7.1 Airfoil nomenclature

of the pressure increase or decrease can be influenced by the radius of curvature. A small radius of curvature causes a rapid acceleration or deceleration resulting in a sharp pressure gradient. A large radius of curvature results in smaller pressure gradients. In addition to the effect of the curvature, the boundary conditions at the leading and trailing edge also have a large effect on the velocity distribution. A stagnation point should be present near the leading edge (velocity is zero). At the trailing edge the Kutta condition should be satisfied. In theory this should result in a second stagnation point at the trailing edge for any airfoil having a finite trailing edge angle. In practice we see that the flow velocity at the trailing edge takes a value closer to the freestream velocity.

To study the variation of pressure distribution about an airfoil we first define the major parameters that characterize each airfoil shape. These parameters are shown in Fig. 7.1. The main dimensions of the airfoil are governed by its maximum thickness ($t_{\max}$) and its chord length, c. Their ratio is often referred to as the thickness-to-chord ratio and abbreviated with t/c. The mean camber line of the airfoil is formed by the locus of points halfway between the upper and lower surface measured perpendicular to the camber line itself. The most forward and rearward points of the camber line are the leading and trailing edge, respectively. The chord line is a straight line connecting these points. The camber is the distance between the chord line and the camber line as measured perpendicular to the chord line. Finally, the curvature of the leading edge can often locally be approximated by a circular arc with a particular radius. We call this the leading edge (or nose) radius of the airfoil, R. The leading-edge sharpness is often represented by the value of Δy, which is also defined in Fig. 7.1 and expressed as a fraction of the chord length.

We first look at two different symmetric airfoils under 6° angle of attack. We evaluate the pressure distribution over these airfoils by using a vortex panel method in combination with a separate boundary-layer model based on the Von Kármán's integral equation (6.89).[1] The two airfoils under consideration are the NACA 0006 and NACA 0018. These airfoils have their maximum thickness at 30 % and have a t/c of 6 and 18 %, respectively. The airfoils and their associated pressure distributions

[1] The program that is used for this evaluation is Xfoil version 6.94. XFOIL carries out a vortex-panel analysis of subsonic isolated airfoils and has the option to include a boundary layer. More information can be found on http://web.mit.edu/drela/Public/web/xfoil/.

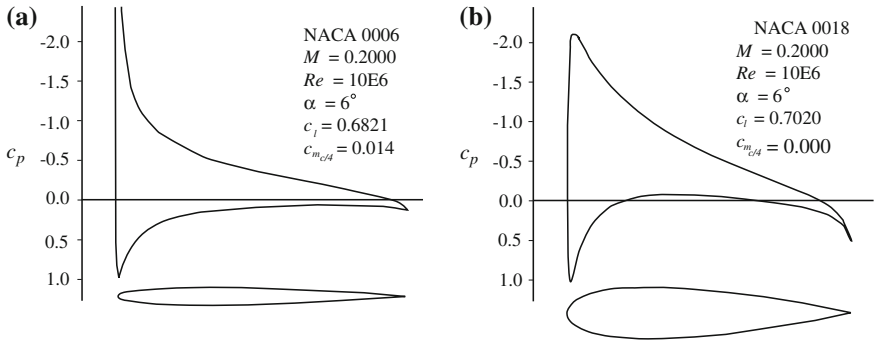

Fig. 7.2 Comparison of pressure distribution between two airfoils of different thickness as simulated by Xfoil version 6.94. **a** NACA 0006. **b** NACA 0018

have been plotted in Fig. 7.2. The aerodynamic coefficients of each of the airfoils are displayed next to the pressure distribution.

Let us start with the similarities between the two airfoils. First of all, they are both symmetrical, which means their camber is identical. Classical airfoil theory tells us that the lift curve slope for a symmetrical airfoil should equal $\mathrm{d}c_l/\mathrm{d}\alpha = 2\pi$. Since we know that for this airfoil $c_l = 0$ at $\alpha = 0$ we expect c_l to be close to 0.66 for $\alpha = 6°$. Comparing that to the value shown in Fig. 7.2a, b we see that the lift coefficient for both airfoils are close to this value, meaning that both airfoils generate almost the same amount of lift. Secondly, we look at the moment coefficient about the quarter-chord point. Assuming classical airfoil theory this value should be zero for both airfoils. We see that this is indeed the case for the NACA 0018, but that the NACA 0006 displays a small nose-up pitching moment about the quarter chord.

We have established that both profiles have a similar overall effect on the lift and moment coefficient of the airfoil. Yet their pressure distributions are somewhat different. The thinner profile of the NACA 0006 causes a much higher suction peak over the leading edge of the airfoil. This large suction peak is followed by a relatively sharp adverse pressure gradient that gradually lessens in magnitude further downstream. The thick airfoil is much more blunt. The radius of curvature at the nose of this airfoil is therefore larger resulting in a lower suction peak. The lower suction peak is followed by a shallower adverse pressure gradient. The magnitude of the suction peak can directly be translated to the magnitude of the supervelocities. A high suction peak yields high supervelocities that can become supersonic at relatively low freestream Mach numbers. At $M = 0.2$ the critical pressure coefficient is -16.3 according to Eq. (3.42).

In the previous chapter we have seen that the value of the adverse pressure gradient in combination with Reynolds number determines whether or not the boundary layer separates. Even though that information cannot be extracted from the analysis carried out above, the shape of the pressure distribution can tell us qualitatively where we should expect flow separation to start. For the thinner airfoil the large adverse pressure gradient near the leading edge will become so large with increasing angle of

attack that the boundary layer is likely to separate from the surface close to the leading edge (even though the boundary layer itself is relatively fresh). Leading edge stall is therefore to be expected on this profile. The thicker airfoil shows a more shallow adverse pressure gradient which is likely to separate the flow starting at the trailing edge, where the boundary layer shape factor (H) has its highest value [see (6.63) on p. 305 for the definition of the shape factor]. Typically when H is between 2.4 and 2.6 boundary layer separation occurs. With increased angle of attack this point is likely to move forward leading to a relatively gentle onset of stall. These deductions on the stall behavior of the airfoil are purely conjectural based on the pressure distribution. However, experimental results from Ref. [1] support these conclusions. We will elaborate more on the separation of the boundary layer in low-speed and high-speed conditions in Sects. 7.5 and 7.6, respectively.

The effect of compressibility on the local pressure coefficient has been discussed qualitatively in Sect. 3.2. The Prandtl-Glauert compressibility correction magnifies the value of the pressure coefficient. It has been shown that this correction (or derivatives thereof) can accurately predict the value of the pressure coefficient by simply multiplying this correction factor to the pressure coefficient obtained from an incompressible-flow calculation (see Chap. 3). However, when Mach numbers are increased beyond M_{crit} the compressibility correction loses its accuracy. In Fig. 7.3 it is shown why this correction cannot be applied in transonic conditions. The same airfoil (NACA 0012) is evaluated with two different prediction tools for the same freestream conditions (a constant angle of attack and varying Mach number). The prediction in Fig. 7.3a is based on a vortex panel method (Xfoil) with an embedded compressibility correction. We see that the pressure distributions at low Mach numbers are merely amplified. The graphs in Fig. 7.3b are generated using an Euler solver

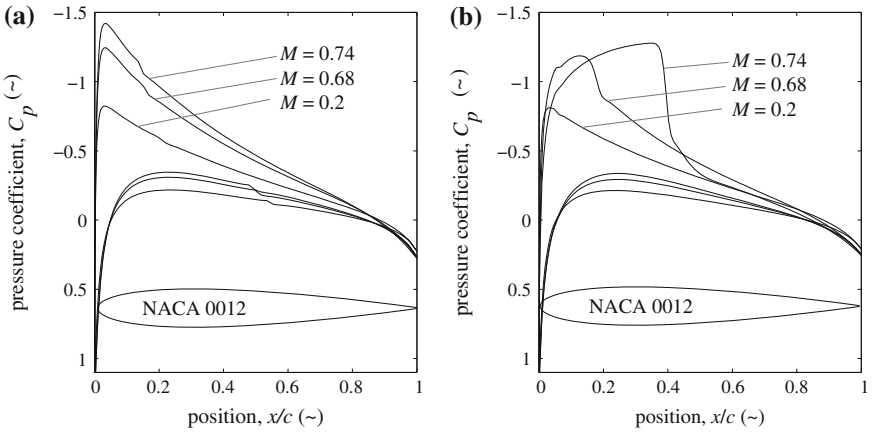

Fig. 7.3 Comparison between results from two prediction tools for the flow over a NACA 0012 airfoil with $\alpha = 2.1$ and $\text{Re}_c = 10$ million. **a** Vortex panel method + compressibility correction (Xfoil v. 6.94). **b** Euler approximation (MES v. 3.04)

(MSES[2]). The graphs of Fig. 7.3b show a distinct change in pressure distribution when the Mach number is $M = 0.68$ or higher. We see how the adverse pressure gradient of Fig. 7.3a is replaced by a more gradual increase in negative C_p in Fig. 7.3b. The steep drop in (negative) C_p is indicative of a shock wave, which is also absent in Fig. 7.3a. This comparison demonstrates the limitation of compressibility corrections in the transonic regime. We will discuss this change in pressure distribution in more detail in Sect. 7.4.

7.3 Laminar-Flow Airfoils

Having looked at the basic characteristics of airfoils we now wonder: what airfoil performs best? Even though this answer might seem simple enough, there exists no one-size-fits all airfoil that performs best for all applications. First of all, what do we quantify as airfoil performance? This question cannot be answered quite straightforwardly. There are a few key performance parameters of an airfoil: its maximum lift coefficient, its lift-curve slope, its lift-do-drag ratio at the design lift coefficient(s), and its moment coefficient at the design lift coefficient(s). The plural form of the lift coefficients already indicates that airfoils are often designed for a range of operating conditions (read: angle of attack and Mach number). Therefore, finding the best airfoil might eventually result in an airfoil that finds the best compromise in performance parameters over the specified range of operating conditions [45].

To maximize airplane range and endurance the lift-to-drag ratio of the airfoil is of relatively high importance. The first efforts to maximize this ratio during the pre-WWII period concentrated on creating large domains of laminar boundary-layer flow over the upper and lower side of the airfoil. At the National Advisory Committee for Aeronautics (NACA) a series was developed for precisely this reason: minimize the drag by generating a favorable pressure coefficient over the upper and lower surface such that the point of transition would be shifted more and more aft. This resulted in the NACA 6-series airfoils that are described in detail in Ref. [1]. These airfoils were designed with a specific lift coefficient in mind. In addition, the position of minimum pressure was specified, indicating the chordwise location of the onset of the adverse pressure gradient. We compare a NACA 6-series airfoil to a NACA 4-series airfoil in Fig. 7.4. Two airfoils of identical thickness are evaluated[3] at identical lift coefficients, Mach numbers, and Reynolds number. Their pressure coefficient and friction coefficient distribution are shown in Fig. 7.4a, b, respectively.

Let us evaluate the results presented in Fig. 7.4. First of all, we would like to emphasize the similarity between the two airfoils: they have the same thickness and

[2] MSES is a viscous-inviscid analysis program that couples the numerical solution of the Von Kármán equation (6.89) in the boundary layer to the numerical solution of the steady state conservative Euler equations (2.183) outside the boundary layer. More information can be found in Refs. [10, 15].

[3] This prediction is carried out by Xfoil 6.94 using an e^N method for transition prediction with $N_{\text{crit}} = 10$.

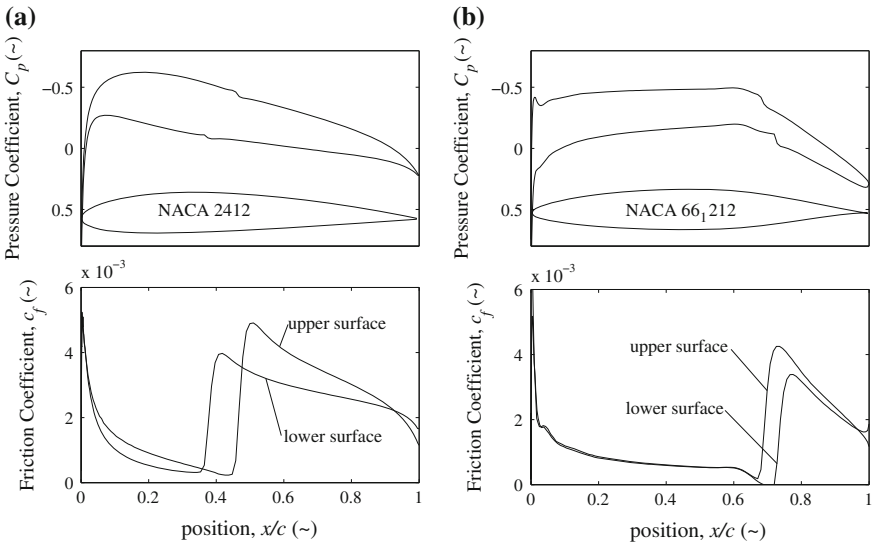

Fig. 7.4 Predicted pressure and shape factor distribution for $c_l = 0.3$, $M = 0.2$, and $\mathrm{Re}_c = 6 \times 10^6$. **a** NACA 2412 at $\alpha = 0.4°$. **b** NACA 66_1212 at $\alpha = 0.9°$

both of them produce the same section lift coefficient. If each airfoil would be used in a separate wing, the structural weight of each wing for a given planform shape would be virtually identical. Even though the integrated difference of the pressure coefficient between upper and lower surface is identical for both wings, their pressure distributions are quite different. The thickest point of the 2412 airfoil is located (by default) at 30 % chord. On the upper surface we see the start of the adverse pressure gradient at approximately $x/c = 0.2$. Transition to a turbulent boundary layer occurs around $x/c = 0.45$. On the lower surface the adverse pressure gradient is slightly steeper and transition occurs closer to the leading edge than on the upper surface. Notice that in this simulation transition can be seen in the jump in the friction coefficient. This indicates where the boundary layer has transitioned from laminar to turbulent. In this particular simulation the step change in displacement thickness that is caused at the transition point can also be seen in the pressure distribution curve by means of a little bump.

The thickest point of the 66_1212 has been shifted beyond the 50 % chord. This creates an almost flat plateau in the pressure distribution over the suction side of the airfoil up the 60 % chord. On the lower surface there is a favorable pressure gradient pressure up to $x/c = 0.6$. Transition occurs on both sides beyond the 60 % chord. Notice the effect of the favorable pressure gradient on the lower side: transition is shifted more aft. We know that the average friction coefficient, C_f is correlated to the integral of the local friction coefficient, c_f, over the chord length. The total area under the two lines in the friction-coefficient diagram are therefore representative for the total amount of friction drag of the profile. Based on that knowledge we can directly see that the total friction drag produced by the 66_1212 is considerably lower

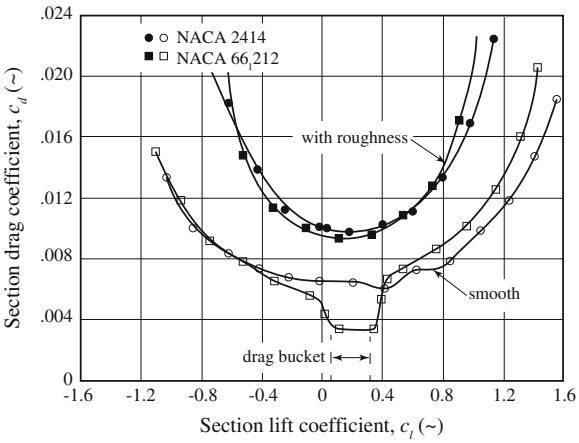

Fig. 7.5 Experimental comparison of drag coefficient between two airfoils at Re $= 6 \times 10^6$ (data from Ref. [1])

than the friction drag produced by the 2412. The predicted drag coefficient is 0.0031 or 31 drag counts[4] for the 66_1212 against 51 counts for the 2412.

Comparison with experimental data of Ref. [1] shows that drag coefficient is somewhat underestimated. In Fig. 7.5 the experimental wind tunnel measurements are presented for a Reynolds number of 6 million. It can be seen that at $c_l = 0.3$ the drag coefficients is around 34 counts for the 66_1212 versus 63 counts for the 2412. We notice a 45 % decrement in drag when switching from a 2412 to a 66_1212. The lift-to-drag ratio of the airfoil is increased with more than 80 % from 48 to 88.

As can be seen from Fig. 7.5, the natural-laminar-flow (NLF) airfoil has a limited range of lift coefficients where the friction drag is low. As a matter of fact, the designation of the airfoil already shows this:

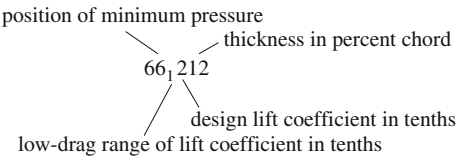

The design lift coefficient is 0.2 and we can expect a low drag coefficient (also known as the *drag bucket*) between $c_l = 0.1$ and $c_l = 0.3$. Outside of the drag bucket the drag of the NLF airfoil is either close to, or higher than the drag coefficient of the NACA 2412. In addition, when the skin is roughened (using NACA standard roughness) the drag coefficient at $c_l = 0.3$ increases to 95 cts while the drag of the 2412 increases to 100 cts, making the difference between the two airfoils very small. This illustrates the sensitivity of both profiles to skin roughness. In practice, roughness can stem from irregularities on the skin, rivets, or waviness in the skin surface. In addition, steps

[4] One drag count equals a drag coefficient variation of 0.0001.

in the surface due the presence of a leading-edge high-lift device or an inspection hatch are also detrimental for laminar boundary layers. Each of them triggers a much earlier onset of transition, increasing the drag dramatically.

In addition to the higher drag outside of the drag bucket, the NACA 66_1212 also has a lower maximum lift coefficient than the NACA 2412. The sharper nose causes an early onset of leading-edge stall, with a maximum lift coefficient of 1.45. The nose of the 2412 has a larger radius and therefore generates a maximum lift coefficient of 1.7 [1].

7.4 Supercritical Airfoils

When the thrust of engines increased with the commercial introduction of the jet engine in the 1950s, it quickly became clear that close to the speed of sound the drag of the airplane increased exponentially (*drag divergence*). The Mach number at which drag divergence starts is often defined as the Mach number at which the numerical value of the slope of the curve of c_d versus M is 0.10 [19]:

$$M_{\mathrm{dd}} = \left(\frac{\partial c_d}{\partial M}\right)_{c_l=\text{constant}} = 0.10 \tag{7.1}$$

This exponential increase in drag was attributed to the formation of strong shock waves on the wing surface in combination with separation at the shock foot. It was found that the natural laminar flow airfoils produced a significant amount of wave drag whenever they were exposed to Mach numbers beyond the critical Mach number (see Fig. 7.6a). This limited the maximum Mach number of early jet fighters

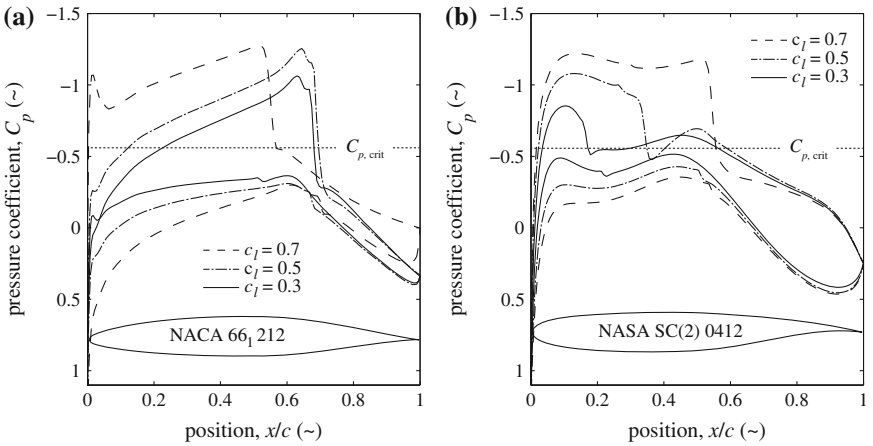

Fig. 7.6 Predicted pressure distribution for $c_l = 0.3$, $c_l = 0.5$, and $c_l = 0.7$ at $M = 0.75$, $\mathrm{Re}_c = 20 \times 10^6$. **a** NACA 66_1212. **b** NASA SC(2) 0412

that used NACA 6-series airfoil sections. One effort to tackle this problem was to investigate whether airfoil shapes could be developed that would have a higher critical Mach number in combination with lower wave drag in *supercritical* (i.e. $M_{\text{local}} > 1$) conditions. In the United Kingdom it was H.H. Pearcey that investigated new airfoil shapes that would allow for supersonic flow on the upper surface of the airfoil without a strong terminating shock wave [35]. In the Unites States under the supervision of R.T. Whitcomb a new family of supercritical airfoils was developed specifically designed to produce low wave drag at high Mach numbers [17]. The pressure distribution of one of these airfoils is shown in Fig. 7.6b.

If we compare the pressure distributions between the NLF airfoil and the supercritical (SC) airfoil of identical thickness, we see a large difference on both the upper and lower surface. In the graph for the NLF airfoil we already recognize the presence of a shock wave at $c_l = 0.3$ (remember that this c_l is still the low-speed design range for this airfoil). We recognize the shock wave by the sharp increase in C_p close to $x/c = 0.6$. If we look at the SC airfoil we see that the suction over the upper surface is much lower at $c_l = 0.3$. Most of the lift for this airfoil stems from the difference in pressure on the aft part of the airfoil. The concave shape of the lower surface causes an increase in pressure on the lower surface which makes a large contribution to the total lift coefficient. We call this *aft loading* and it is one of the means to lower the required supervelocities on the upper surface of the airfoil for a given lift coefficient (see Problem 7.2). When the lift coefficient is increased to 0.5 the shock wave on the NLF airfoil increases in strength (larger pressure rise). On the SC airfoil we also see the formation of a shock wave around $x/c = 0.35$. However, the latter shock wave is much weaker than the one over the NLF airfoil as can be observed from the smaller pressure increase. Finally, at $c_l = 0.7$ the shock over the NLF airfoil has shifted forward, while its strength has remained approximately the same. However, the trailing-edge C_p has now become substantially more negative, indicating that the boundary layer has separated from the trailing edge. On the SC airfoil we see that the shock has moved aft and has increased in strength. There is no indication of boundary layer separation.

In Fig. 7.7 the corresponding curves for the drag coefficients are shown. Notice that the drag coefficient (on the vertical axis) has been expressed in terms of drag counts. The drag coefficient consists of two fundamental components: the friction drag coefficient, c_{d_f}, and the pressure drag coefficient, c_{d_p}. In this analysis the pressure drag coefficient has been found by integrating the pressure over the section and projecting the resulting force vector onto the direction of the flow.[5] If we compare the drag coefficient development between the two airfoils, we immediately see that the NLF airfoil shows a sharp increase in drag coefficient between $c_l = 0.3$ and $c_l = 0.5$. Since the friction drag is almost constant, this increase in drag is almost solely due to the formation of a strong shock wave on the upper surface. The SC airfoil shows almost a constant value for the total drag coefficient over this range. At $c_l = 0.5$ the drag of the SC airfoil is therefore 37 % lower than for the NLF airfoil. At $c_l = 0.7$ the shock has become significantly stronger, which results in an increase

[5] This calculation procedure for obtaining the pressure drag is often called a "near-field analysis".

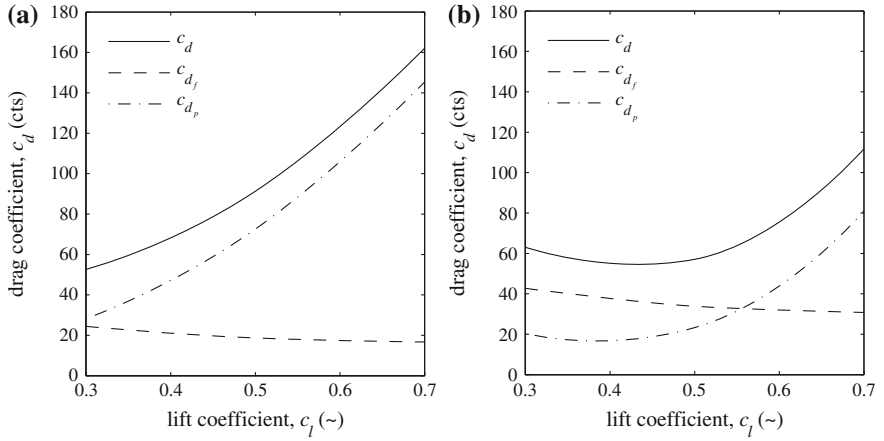

Fig. 7.7 Predicted drag coefficients at $M = 0.75$, $\mathrm{Re}_c = 20 \times 10^6$. *Note* c_{d_p} indicates pressure drag, while c_{d_f} indicates friction drag. **a** NACA 66_1212. **b** NASA SC(2) 0412

in pressure drag. However, the flow remains attached and the pressure drag does not rise as fast as for the NLF airfoil.

For a given airfoil shape, the thickness ratio (t/c) and lift coefficient are often the most important parameters that influence the drag divergence Mach number. Figure 7.8 shows how for supercritical and NACA airfoils the thickness ratio influences the drag-divergence Mach number. According to this graph, for supercritical airfoils, the drag-divergence Mach number decreases linearly according to the following statistical relation:

$$M_{\mathrm{dd}} = 0.92 - 1.16\left(\frac{t}{c}\right) \quad \text{for} \quad c_l = 0.5 \tag{7.2}$$

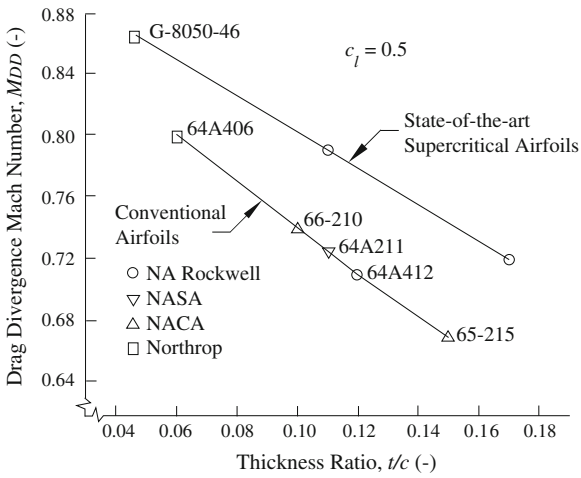

Fig. 7.8 Effect of thickness ratio on drag divergence Mach number for NACA and supercritical airfoils (after Ref. [37])

The decrease in drag divergence Mach number can be explained by the fact that the thicker airfoils create higher supervelocities over the upper and lower surface than a thin airfoil. A thicker airfoil will therefore encounter critical conditions at a lower free stream Mach number than a thin airfoil. In general, this also results in an earlier onset of shock-induced boundary-layer separation and therefore drag divergence.

In Fig. 7.9 we show an example of the effect of lift coefficient on the drag divergence Mach number. The drag divergence Mach number in this graph is defined as the point on the line where $\partial c_d/\partial M = 0.10$. We can observe that with increasing lift coefficient the drag divergence Mach number decreases. This can be explained by the fact that the increase in lift coefficient is a result of higher supervelocities on the suction side of the airfoil, which causes an earlier formation of the shock wave and associated shock-induced separation. A rudimentary equation to compute the drag divergence Mach number that includes both the thickness-to-chord ratio and the lift coefficient is given by Korn:

$$M_{\mathrm{dd}} + t/c + 0.10 = \kappa \tag{7.3}$$

where κ is a technology factor that amounts to 0.95 for supercritical airfoil sections. Torenbeek [44] derived a modified version of Korn's equation based on empirical data of second generation supercritical airfoils [17]:

$$M_{\mathrm{dd}} + t/c + 0.10 c_l^{1.5} = M^\star \quad \text{with} \quad M^\star = 0.935 \tag{7.4}$$

It should be emphasized that a different airfoil shape can highly influence the dependency of the drag divergence Mach number to the lift coefficient. It was already shown by Göthert in 1944 that careful modification of a NACA 0012 could yield a constant drag divergence Mach number of 0.78 for a lift coefficient ranging from 0 to 0.4 [16]. Blackerby and Johnson show in Ref. [7] that changing the forward 12 % of the airfoil can have a profound effect on the drag divergence Mach number.

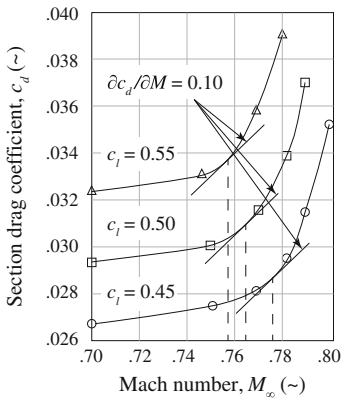

Fig. 7.9 Effect of lift coefficient on drag divergence Mach number for the Lockheed C141A airfoil at 38.9 % of the semi span (data from Ref. [7])

7.4.1 Shock-Free Supercritical Airfoil

What we now know as a supercritical airfoil was still to be discovered in the early 1960s. In a 1963 paper on the development of low-drag SC airfoils, Pearcey states the questions that needed to be answered at the time [35]: "Just how much can the velocity be allowed to exceed sonic locally without incurring strong, drag-producing shock waves, and how does this in turn depend on the velocity distribution and section shape?" Keeping in mind that numerical tools such as those employed in this chapter were unavailable at this time and that the analytical methods to predict subsonic pressure distributions were inadequate for transonic flow, these questions could only be answered through a thorough experimental investigation. The goal of this investigation was to find a section shape that would allow for supersonic flow to develop over the top surface but without the drag-producing shock wave. One of the key findings of this investigation was a clear elaboration on the effect of the expansion waves generated at the leading edge of the airfoil. We will follow this elaboration (Ref. [35]) to demonstrate the complex interaction of expansion and compression waves in the supersonic domain of the flow.

We first consider a generic airfoil in high subsonic conditions (Fig. 7.10). The flow over the airfoil accelerates to beyond $M = 1$, which introduces a supersonic flow domain on the upper side of the airfoil. The line separating this *supersonic bubble* from the subsonic domain is called the *sonic line*. This sonic boundary forms a constant pressure surface and attaches to the airfoil close to the leading edge (at the point where the flow accelerates locally beyond $M = 1$). We assume that right behind this line an expansion wave (left-running Mach wave) is generated by a small disturbance. This wave travels through the supersonic flow field until it reaches the sonic line. Since expansion waves cannot travel in the subsonic flow domain outside the sonic line, it is reflected towards the surface. Because the sonic line is a constant-pressure surface the expansion wave is reflected as a compression wave (*reflection in unlike sense*). The supersonic flow in between the expansion wave and the compression wave experiences an increment in Mach number (ΔM) due to

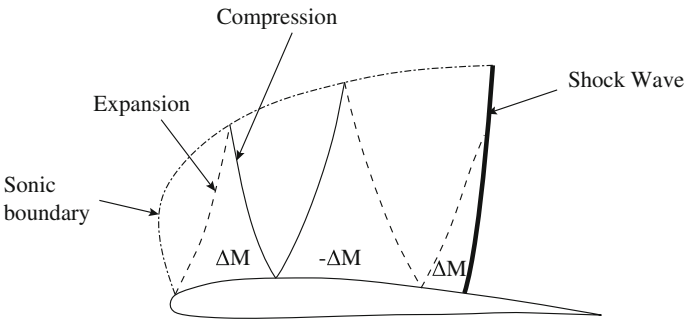

Fig. 7.10 Notional reflection of a single expansion wave emanating close to the leading edge (after Ref. [35])

the expansion wave. The flow behind the reflected compression wave experiences a decrement in Mach number of equal strength. The resulting Mach number behind this compression wave would therefore be equal to the Mach number in front of the first expansion wave.

When the compression wave reaches the airfoil surface it is being reflected. If the surface is flat the compression wave is reflected as a compression wave (*reflection in like sense*). However, if the surface has sufficient convex curvature, the flow tangency condition requires the streamline to bend towards the surface and the incident compression wave is reflected as an expansion wave. Alternatively, the surface can have exactly the right amount of convex curvature such that there is no reflection from the wall. To decelerate the flow it is beneficial to reduce the convex curvature such that the reflected wave is also a compression wave. This has been implicitly assumed in the notional sketch of Fig. 7.10. The flow behind this second compression wave has a lower Mach number than the flow in front of the first expansion wave ($-\Delta M$ in Fig. 7.10). The compression waves therefore aid in the reduction of the Mach number further downstream over the airfoil. Because this compression process is isentropic it is termed *isentropic recompression*.

In reality the single expansion wave should be replaced by an infinite number of expansion waves that emanate from the convex surface close to the leading edge and possibly also further downstream on the airfoil. This expansion fan is reflected from the sonic boundary as a compression fan. The expansion waves and compression waves are intersecting. This is visualized in Fig. 7.11 where the expansion waves are shown as characteristics. We see the expansion characteristics as dashed lines and the compression characteristics as solid lines. In the lower graph the Mach number distribution is shown, where ω is the Prandtl-Meyer angle corresponding to the local Mach number of the flow. In this graph the upper dashed line shows the Mach number distribution if only the expansion waves would be taken into account. Due to the reflection of the compression waves from the sonic line and subsequently from the crest, it can be seen how the Mach number is lowered.

In Ref. [39] it is described that the formation of a shock is the result of a coalescence of the recompression characteristics. If the reflected compression waves coalesce, they merge to form a shock wave. If even a short segment of the profile is straight-sided (instead of convex) a shock will be formed as the result of a coalescence of the compression waves reflected from this segment. In Fig. 7.12 we see two airfoils and their pattern of characteristics. The airfoil in Fig. 7.12a has been designed to be shock free. In other words, the recompression waves emanating from the sonic line do not coalesce in the physical plane. This can only happen if the shape of the sonic line and the flow deflection are carefully tailored to each other [39]. If only a small disturbance travels downstream along the reflected Mach waves it will result in their coalescence: a shock (Fig. 7.12b). This shows how carefully the airfoil geometry must be arranged in order to obtain shock-free supersonic flow.

Pearcey demonstrated experimentally that even subsonic flows that locally accelerate up to $M = 1.4$ can be decelerated isentropically without the formation of a shock. To achieve these properties the airfoil had to have the following properties [35]:

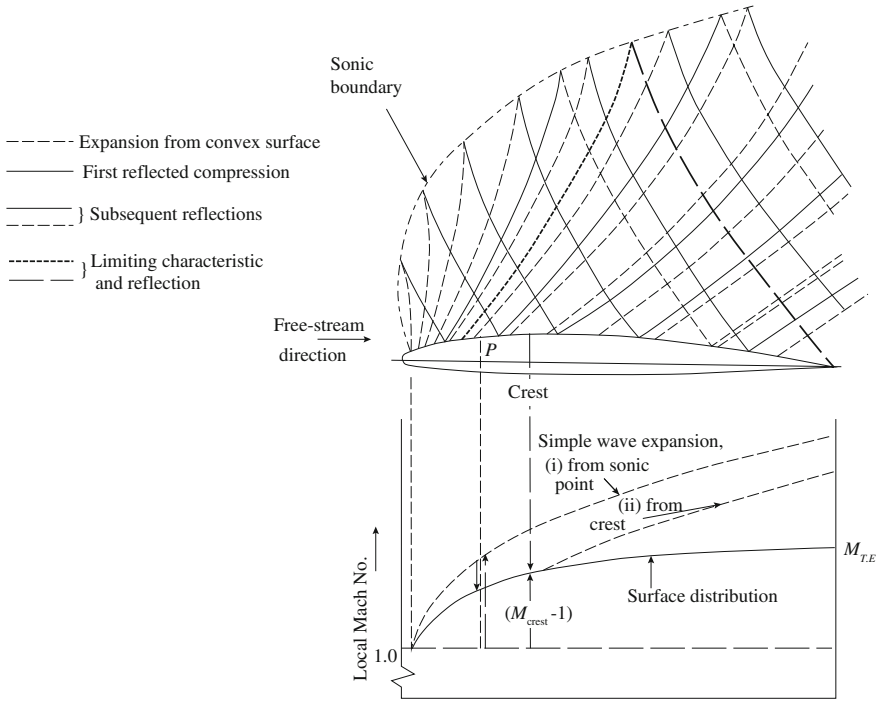

Fig. 7.11 Sketch of Mach-wave pattern in a region of supersonic flow over an airfoil and the Mach number distribution resulting from the supersonic position of the first simple wave, ω_1, and the compressive effect, ω_2 (after Ref. [33])

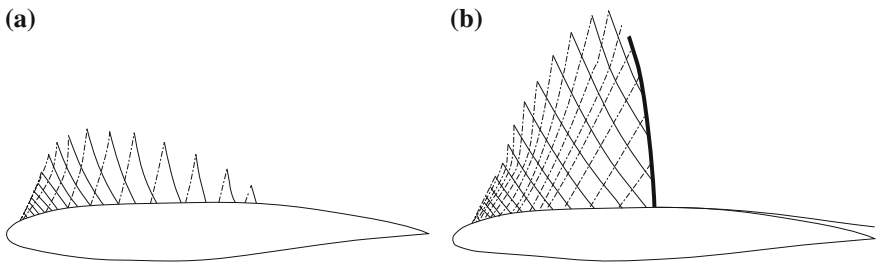

Fig. 7.12 Pattern of characteristic waves over two airfoils (after Ref. [39]). **a** Shock-free. **b** Coalescence causes shock

(a) a sharp suction peak needs to be present at the leading edge during subsonic flow conditions at a particular angle of attack
(b) behind the suction peak rapid deceleration has to occur in subsonic flow, and
(c) behind the leading edge the curvature distribution of the upper surface has to be such that the expansion waves in the supersonic region, the sonic line, and the reflected compression waves are formed behind the suction peak.

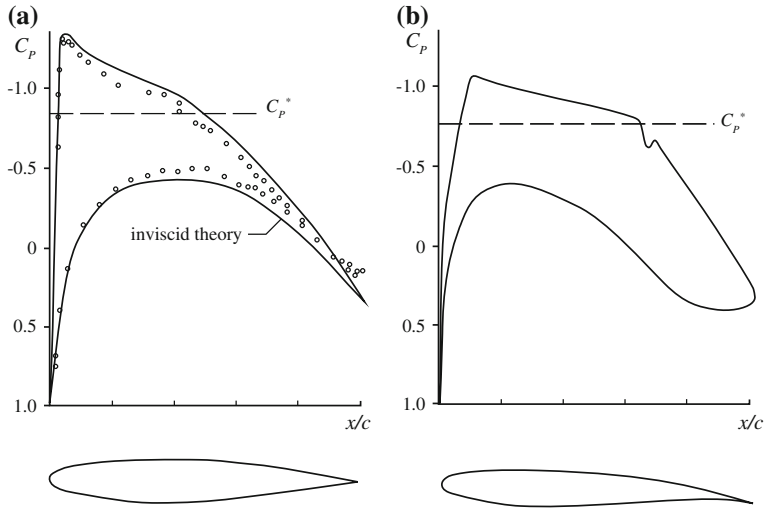

Fig. 7.13 Pressure distribution about a two different shock-free airfoils. **a** $M = 0.709$, $\alpha = 3.6$ (modified from Ref. [8]). **b** $M = 0.765$, $c_l = 0.58$, $\mathrm{Re}_c = 21 \times 10^6$ (after Ref. [23])

Due to the sharp suction peak and high adverse pressure gradient in the subsonic pressure distribution these airfoils are often termed 'peaky' airfoils. Pearcey showed that the significant amount of isentropic recompression could result in shock-free airfoils or airfoils with a weak normal shock wave terminating the supersonic domain. Other researchers (e.g. [8, 23, 39]) demonstrated the potential and limitations of shock-free supercritical airfoils. Figure 7.13 shows the pressure distribution for two of such airfoils. In both graphs the critical C_p has been indicated with a dashed line. We see that both airfoils show a smaller adverse pressure gradient allowing for a larger supersonic bubble. According to Ref. [32] one can expect that for given values of lift coefficient and thickness ratio, the design Mach number for shock-free airfoils will be generally somewhat lower for the peaky designs than for the "nonpeaky" designs of Fig. 7.13. However, this does not necessarily mean that these nonpeaky airfoils also have a higher drag divergence Mach number. On the contrary, they have been shown to be more sensitive to off-design conditions than peaky airfoils.

We have now shown that shock-free airfoils have the possibility of producing relatively high lift coefficients (around $c_l = 0.6$) without producing any wave drag. In theory this is an ideal solution. However, in practice these airfoils are hardly used on high-subsonic transport aircraft. One of the main reasons for this is their sensitivity to changes in the flow condition. These could stem from a change in Mach number, angle of attack, or even Reynolds number. This is illustrated for the Garabedian-Korn airfoil of Fig. 7.13b in Ref. [21] where the airfoil is predicted[6] to be shock free for $M = 0.751$ and $c_l = 0.625$ while for $M = 0.750$ and $c_l = 0.629$ it is predicted to have two shocks. In reality the displacement effect of the boundary layer also plays

[6] The prediction was made by assuming the flow to be inviscid (Euler solution).

an important role in whether the shock-free condition can be attained. Given the fact that the displacement thickness is dependent on the Reynolds number it is very well possible that an airfoil shows to be shock-free in the wind tunnel while having a weak shock during flight for the same Mach number and lift coefficient.

7.4.2 Supercritical Airfoils with Shocks

The 'peaky' airfoil sections of Pearcey proved to be able to produce shock-free pressure distributions. Even with increases in Mach number and lift coefficient these airfoils proved to produce relatively weak shock waves. At NASA the work of Pearcey had not remained unnoticed and under the leadership of Richard Whitcomb a series of supercritical airfoils were developed (of which an example is shown in Fig. 7.6b). The goal was to develop an airfoil which would have acceptable drag characteristics at Mach numbers significantly beyond the critical Mach number. The first airfoil was a 13.5 % thickness airfoil (NACA 64A series, see Ref. [1]) that exhibited a slot close to the trailing edge (see Problem 7.5). With a design lift coefficient of 0.65, the drag-divergence Mach number increased from $M = 0.67$ for the airfoil without slot to $M = 0.79$ for the slotted airfoil [47].

Even though the slotted airfoil performed well in terms of drag rise postponement, there were a number of disadvantages associated with this concept. It introduced additional structural complexity in the design as well as increased friction drag. In addition, it was found that the curvature of the lower surface near the slot was extremely critical and close to dimensional tolerance [17]. Therefore, work proceeded to find airfoil shapes that had the same high-speed characteristics as the slotted airfoil but consisted of a single element. From an aerodynamic point of view the design of the upper surface was to be such that the compression and expansion waves would balance each other to get an airfoil with a flat pressure distribution even though there would be continuous curvature over the upper surface.

There are two primary factors that influence the balance of these waves: the leading edge radius and the upper surface curvature up to the mid chord. A strong expansion is required over the leading edge of the airfoil such that these waves can be reflected back as compression waves. This is done by making the leading edge thicker (blunter). The leading edge of a typical transonic airfoil has a radius of curvature which is twice as large as for NACA 6-series airfoils of the same thickness-to-chord ratio. The rounded nose of the airfoil is beneficial at low speeds too, because it reduces the suction peak at the nose and, hence, delays stall, thereby improving take-off and landing characteristics [4]. Secondly, the curvature of the mid-chord region must be fairly small to reduce the strength of the expansion waves that emanate from this convex surface (see Fig. 7.11). The curvature should be such that the emanating expansion waves and reflected compression waves are balanced. Hence the flattened upper surface of many supercritical airfoils. Finally, the lower surface aft of the mid chord shows distinct cambering to generate the aft loading. This results in an increased nose-down pitching moment and also reduces the available space for

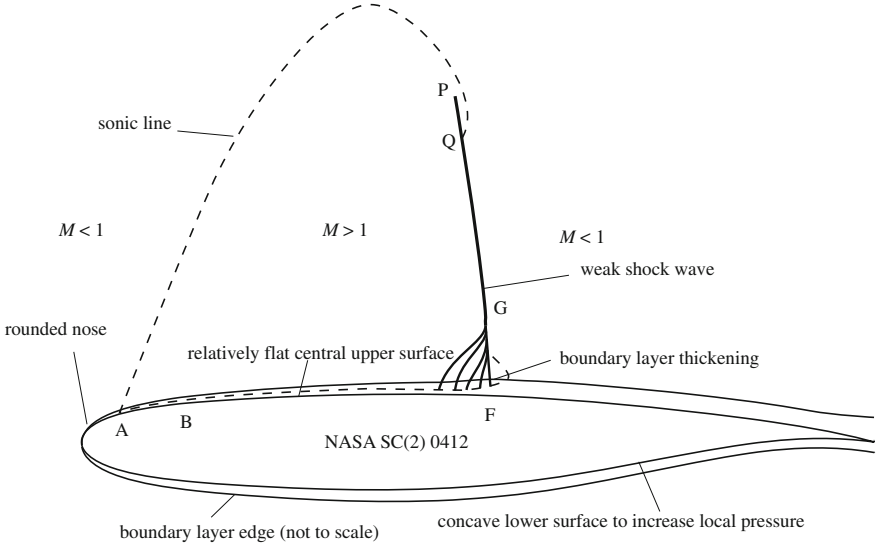

Fig. 7.14 Typical geometry and characteristics of a supercritical airfoil

the (flap) structure. Figure 7.14 shows the geometric characteristics of a 12 % thick supercritical airfoil.

In addition to the geometric characteristics, Fig. 7.14 also shows key aerodynamic properties of a supercritical airfoil. A notional boundary layer thickness has been drawn for reference. We see that the sonic line, which separates the two flow domains, forms a continuous boundary around the supersonic bubble. We see that the shock wave is slightly curved. The tip of the shock (point P) is in the supersonic domain. The curved part of the shock (oblique with respect to the local flow direction) causes the flow decelerate to a Mach number higher than unity, causing a small supersonic region behind this part of the shock. The flow decelerates isentropically to subsonic conditions in this region. The sonic line therefore attaches to the shock at point Q. Below point Q the shock is normal to the local flow direction and the flow decelerates to subsonic conditions. If we move towards the foot of the shock (point F) we see that the shock is formed by the coalescence of compression waves that smear the pressure increase over a finite interval. Due to this pressure increase, the boundary layer thickens (as is explained in Sect. 6.4.3).

Most modern jet transports employ supercritical airfoils or use some form of supercritical geometry in their airfoil design. For example, all the Airbus aircraft employ supercritical airfoils, as do the latest Boeing aircraft (777, 787). Other Boeing aircraft (e.g. 737-700 and 767) also include airfoils that are modified using supercritical airfoil technology [4].

Example 7.1 Consider an aircraft that performs an accelerated climb from $M = 0.50$ to $M = 0.77$ while the lift coefficient of the aircraft remains constant. At 70 % semi-span the wing has a DSMA-523a supercritical airfoil with a thickness-to-chord ratio

of 11 %, developed by McDonnel Douglas (see below). To investigate the aerodynamic phenomena at that spanwise location, you are asked to perform a two-dimensional aerodynamic analysis for a constant lift coefficient of $c_l = 0.85$. This includes the pressure distributions over the airfoil at the Mach numbers $M = 0.50$, $M = 0.73$ and $M = 0.77$ and the corresponding moment coefficients and drag coefficients.

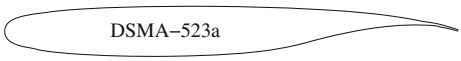

Solution:

First we need to chose a suitable solver for this question. Since we know that the flow about a supercritical airfoil in high-subsonic conditions will be mixed (both subsonic and supersonic domains) we choose a numerical approximation of the Euler equations. In this case we use a finite-volume approximation of the Euler equations on an unstructured grid. A detailed description of this approximation can be found in Ref. [9]. Since these calculations are based on the assumption that the flow is inviscid, we will not be able to deduce any viscous effects such as separation. In addition, the exact shock position is most likely to be somewhat inaccurate due to the lacking shock wave-boundary layer interaction (SWBLI). However, it does give a good insight into the development of the shock wave and its position and gives a reasonable prediction for high Reynolds-number flows, such as found over high-subsonic transport aircraft. It is therefore found to be a suitable tool to determine the pressure distributions about this airfoil. The results for the prescribed conditions are found in Fig. 7.15. Note that these plots show the input values above the graph: Mach number and angle of attack. The output in terms of aerodynamic coefficients is displayed within the plot. To keep the lift coefficient constant at each Mach number we performed several iterations where we changed the angle of attack, until the result showed a lift coefficient close to the target of $c_l = 0.85$.

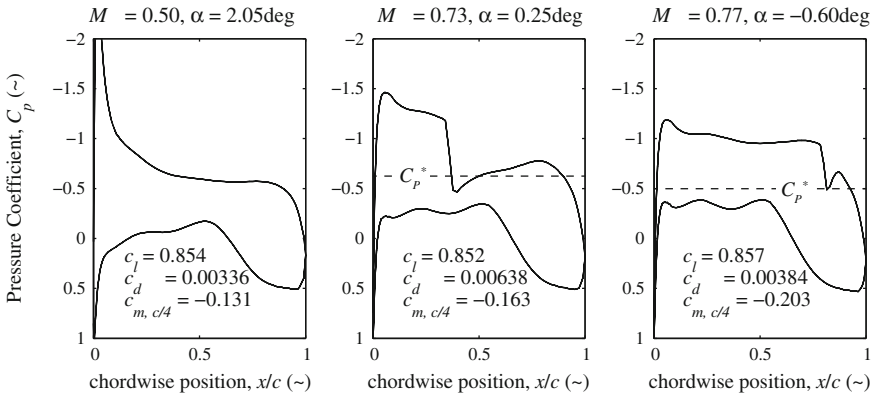

Fig. 7.15 Development of pressure distribution with constant lift coefficient and increasing Mach number over a DSMA-523a airfoil. *Note* this is the result of an inviscid calculation, hence $c_d = c_{d_p}$

Let us analyze the changing pressure distribution of Example 7.1. First we consider the effect of the increasing Mach number on the pressure distribution over the airfoil while the lift coefficient remains constant (see Fig. 7.15). In the left graph we see the expected peaky behavior of the supercritical airfoil at low-speed conditions. The suction peak at the leading edge is followed by a relatively sharp adverse pressure gradient, due to the lack of curvature on the top side of the airfoil. We also identify the aft loading, which is caused by the concave shape of the lower side of the airfoil over the aft 40 %c. When the freestream Mach number goes beyond the critical Mach number, a plateau is formed in the pressure distribution. This represents the supersonic domain of the flow and is terminated by a sharp pressure increase: the shock wave. As we increase the freestream Mach number even more the shock wave starts to move backwards towards the trailing edge, while the crest of the pressure distribution lowers. Notice that by only increasing the Mach number by 0.05, we now have more than 85 % of the top surface emersed in supersonic flow. Also note that the pressure distribution over the bottom side of the airfoil hardly changes. The flow is fully subsonic there and we only distinguish a magnification of the pressure coefficient between $M = 0.5$ and $M = 0.73$ due to compressibility effects. Furthermore, we see that the drag coefficient decreases when the Mach number increases from 0.73 to 0.77. This large decrease is rather unrealistic and is attributed to the absence of viscosity in the flow solver. Finally, we would like to point out the rapid change in moment coefficient about the quarter chord point. In subsonic conditions we would expect the moment coefficient to stay constant about this point. It is clear from the values for $c_{m,\,c/4}$ that the nose-down pitching moment increases substantially. This phenomenon is often referred to as *Mach tuck* or *tuck under*. To compensate for this and balance the aircraft around its center-of-gravity, we need to apply a larger nose-up pitching moment. For a conventionally configured airplane this is achieved by providing more downforce on the horizontal stabilizer, which increases the trim drag.

Example 7.2 Consider an aircraft that is flying at a constant Mach number of $M = 0.732$. The airfoil at 70 % semispan is again the DSMA-523a supercritical airfoil. A coordinated turn (no side-slip) at constant Mach number and altitude requires a change in lift coefficient of the wing, and therefore on the wing section. To investigate the aerodynamic phenomena, you are asked to do a two-dimensional analysis. This includes the calculation of the pressure distribution about the DSMA-523a airfoil at a constant Mach number of $M = 0.73$ and the following lift coefficients: $c_l = 0.5$, $c_l = 0.9$, and $c_l = 1.1$. In addition, you are asked to calculate the moment coefficient about the quarter chord and the wave drag coefficient.

Solution:

Having done the previous example (Example 7.1), we use the same numerical approximation of the steady Euler equations, keeping in mind that we assume the flow to be inviscid. We evaluate the airfoil at the prescribed lift coefficients. However, since the lift coefficient is an output of the calculation (by summing the pressure difference

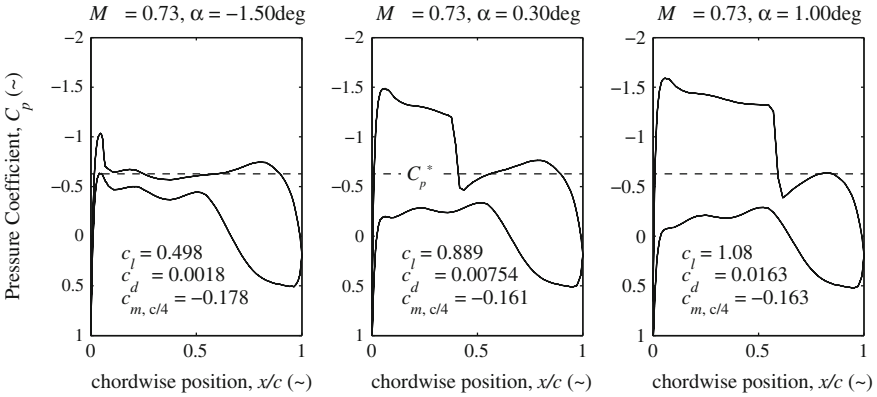

Fig. 7.16 Development of pressure distribution with increasing lift coefficient and constant Mach number over a DSMA-523a airfoil. *Note* this is the result of an inviscid calculation, hence $c_d = c_{d_p}$

between the suction and pressure surface) we need to do this iteratively by varying the angle of attack in the input file. The result is displayed in Fig. 7.16.

In the example above we can distinguish the effect that changing lift coefficient has on the pressure distribution over the wing. We see that for a relatively low lift coefficient, the main contribution to the lift coefficient comes from the aft loading of the airfoil, which, in turn, produces quite a large nose-down pitching moment about the quarter-chord point. When the lift coefficient increases (through the change in angle of attack), we see that a plateau is formed in the pressure distribution. This plateau rises and becomes longer when the lift coefficient is even further increased. At the same time we see that the shock wave becomes stronger, yielding more wave drag with higher lift coefficient. A quick analysis of the results shows that the average lift curve slope of this airfoil at $M = 0.73$ is $14.1(1/\text{rad})$, which is more than twice the value of what we expect from this airfoil at low speeds, which is around $2\pi = 6.28\,(1/\text{rad})$. This demonstrates that in the present conditions this airfoil is much more responsive to changes in angle of attack, than at low speeds. In practice this means that atmospheric gusts can have a relatively large impact on the pressure distribution over the wing and can hence introduce large fluctuations in wing lift. In the cabin we feel this as if the aircraft is driving on a road dotted with potholes. We will see in Chap. 8 that the introduction of sweep reduces the lift-curve slope of the aircraft and, therefore, partially compensates for this large sensitivity.

The results shown in Examples 7.1 and 7.2 are predictions of an inviscid Euler code. In Fig. 7.17 a Mach and c_l sweep is shown about a supercritical airfoil. Both experimental results obtained in a wind tunnel ($\text{Re}_c = 14.5 \times 10^6$) and numerical results obtained by an Euler code with boundary layer approximation (viscous-inviscid prediction) are shown. If we look at the wind tunnel test results we see a similar behavior as in the results of the aforementioned examples. With increasing Mach number and constant lift coefficient the shock wave moves aft while the minimum pressure coefficient decreases somewhat. When the Mach number is kept

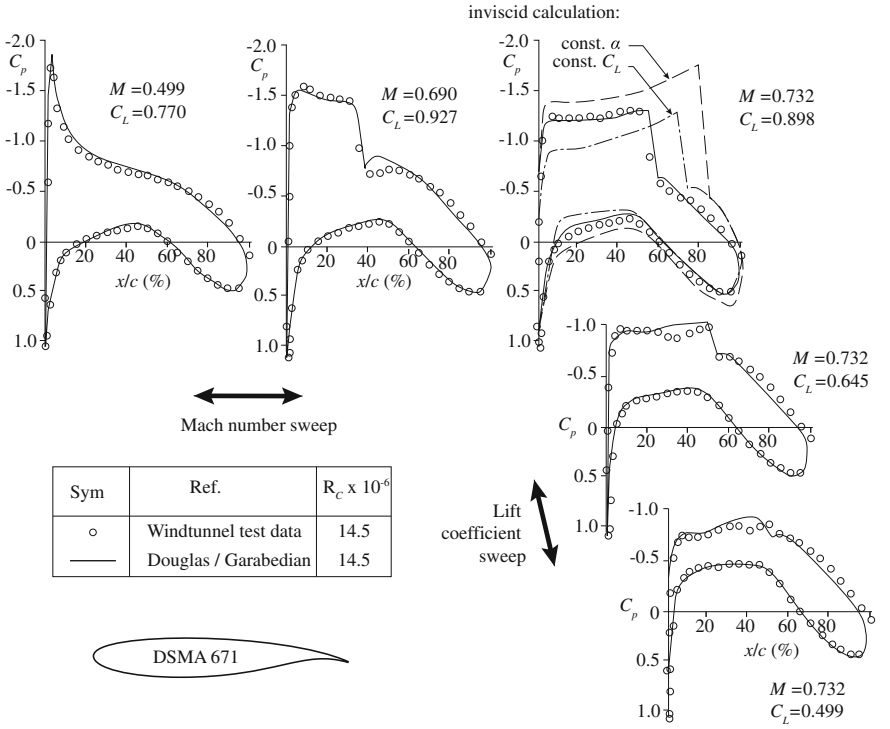

Fig. 7.17 Mach number and c_l sweep for a 14 % thick supercritical airfoil (after Ref. [22])

constant while the lift coefficient is increased, a shock wave starts to form. The plateau in the lift distribution rises with increasing lift coefficient, while the shock position remains almost constant.

Finally, we note that the prediction of the pressure distribution of the viscous-inviscid flow solver is quite accurate. Both position of the shock and the supercritical C_p is accurately predicted. We see in the top right graph of Fig. 7.17 an Euler prediction (inviscid) for two conditions: constant α and constant c_l. This means that the equations are being solved respectively for the same α and c_l as in the wind tunnel experiment. We see that the Euler prediction is unable to properly capture the position of the shock wave. Due to the absence of the displacement thickness of the boundary layer, the higher effective curvature of the upper side of the airfoil generates a higher supercritical Mach number which pushes the shock wave more aft. For the same lift coefficient (constant c_l) and higher Mach number the airfoil is positioned under a lower angle of attack, resulting in an underprediction of the supercritical Mach number. For the evaluation at constant angle of attack, the prediction is even more off: the supercritical speeds are over predicted and the shock wave is too far aft. This combination results in an over estimation of the lift coefficient. The large discrepancy between the Euler prediction and the measured data is evidence that the inclusion of the boundary layer is important to accurately capture the pressure distribution

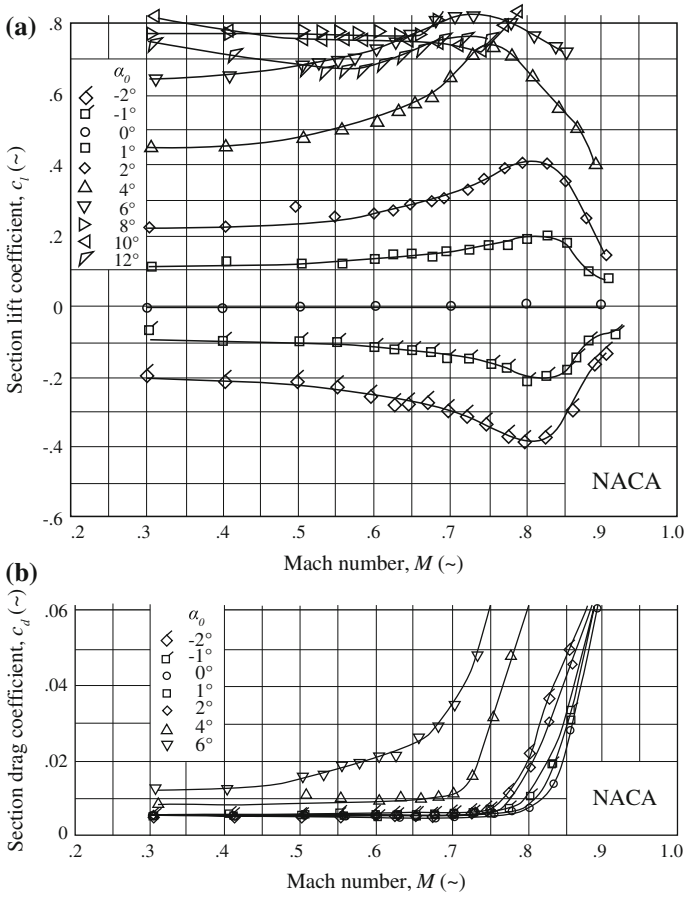

Fig. 7.18 The measured variation of section properties with Mach number of a NACA 64A010 airfoil for various angles of attack [18]. **a** Lift coefficient. **b** Drag coefficient

about supercritical airfoils. The results of Examples 7.1 and 7.2 can therefore not be perceived as an accurate prediction, but merely serve as examples.

The change in lift and drag coefficient with Mach number is shown in Fig. 7.18 for a modified NACA 6-series airfoil of 10 % thickness. In Fig. 7.18a we observe that initially the low-subsonic lift coefficient is amplified by the compressibility effect, in accordance with the compressibility corrections that were introduced in Chap. 3. However, at higher Mach numbers, the formation of shock waves break the amplification trend and with ever higher Mach number, shock-induced separation (see also Sect. 7.6) causes the lift coefficient to drop. At the same time, the drag coefficient due to the presence of the shock wave and shock-induced separation starts to rise. With increased angle of attack, the onset of the drag rise occurs at ever lower Mach numbers, showing that the drag-divergence Mach number is a function of both

Mach number and angle of attack. This behavior is not unique to this specific airfoil but applies to most supercritical airfoils. The higher the required lift coefficient, the higher the angle of attack needs to be to achieve that. With higher angle of attack, higher supervelocities on the upper surface of the airfoil are encountered, resulting in an earlier onset of shock waves and shock-induced separation.

7.4.3 Sonic Rooftop Airfoils

Whereas on supercritical airfoils the supersonic region on the upper surface of the airfoil is terminated with a weak shock, so-called 'sonic rooftop' airfoils lack a supersonic region all together. The 'sonic rooftop' refers to the sonic flow over the first part of the airfoil, similar to the supersonic region on a supercritical airfoil. A sonic rooftop airfoil is designed for transonic speeds, but such that the flow at the *design condition* just reaches sonic speeds over the flat region of the upper surface. This implies that a terminating shock wave is absent and wave drag amounts to zero in the design condition. The drag divergence Mach number for sonic rooftop airfoils is higher than for supercritical airfoils. However, this does come at an expense. Sonic rooftop wings are thinner and, consequently, hold less fuel. They also require a heavier structure to transfer the bending moment in the wing. Furthermore, the nose radius is smaller which decreases their maximum lift coefficient at low speeds.

In Fig. 7.19 we compare two airfoils of similar but different geometry. One is designed as an SC airfoil with a design lift coefficient of 0.635, while the second airfoil is a sonic rooftop airfoil with a design lift coefficient of 0.500. Both airfoils have a design Mach number of 0.72. Their respective pressure distributions are shown in Fig. 7.19a, b. The sonic rooftop profile of the pressure distribution is clearly visible in Fig. 7.19b. If we compare the two drag components of each airfoil we see that the friction drag is predicted to be the same, while pressure drag of the SC airfoil is 10 drag counts higher than for the sonic rooftop airfoil. The lift to drag ratio of the SC airfoil in the design condition is $c_l/c_d = 78$, while for the sonic rooftop airfoil this value is estimated to be $c_l/c_d = 70$. Looking at Fig. 7.19c we see that the drag divergence Mach number is higher for the sonic rooftop airfoil than for the SC airfoil. Furthermore, we distinguish in this figure the relative geometry of both airfoils which corresponds to the description of the previous paragraph.

7.4.4 Effect of Trailing Edge Geometry

One important characteristic of the pressure distribution over the upper surface of a supercritical airfoil is the strong adverse pressure gradient that exists over the aft part of the airfoil. We know from Chap. 6 that the boundary layer is more susceptible to separate under a strong adverse pressure gradient. Therefore transonic airfoils are often designed to reduce this adverse pressure gradient by incorporating two

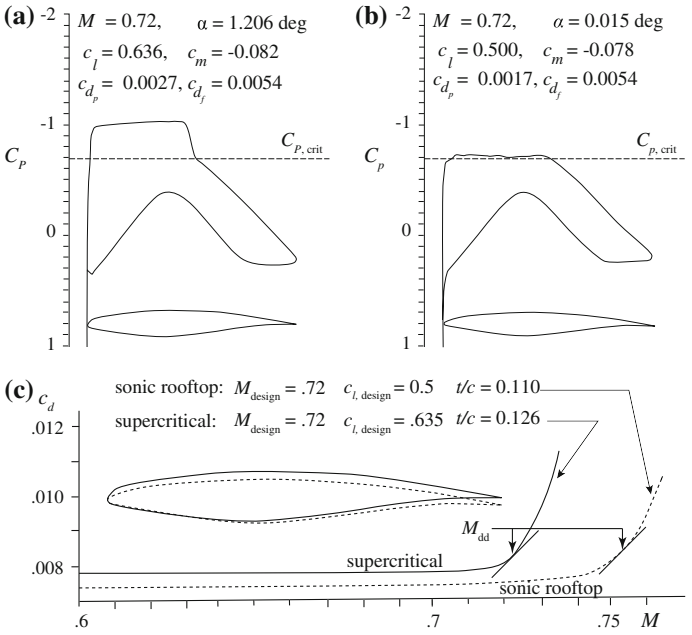

Fig. 7.19 Comparison between a supercritical and a sonic rooftop airfoil of similar but different geometry (after Ref. [33]). *Note* c_{d_f} indicates friction drag while c_{d_p} indicates pressure drag. **a** Supercritical airfoil. **b** Sonic rooftop airfoil. **c** Drag coefficient versus Mach number

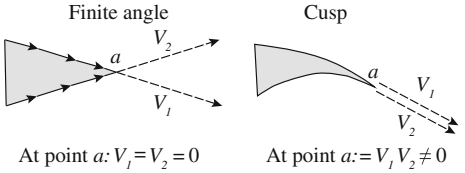

Fig. 7.20 Trailing edge shapes relating to the Kutta condition (after Ref. [3])

geometric measures: a cusp trailing edge, and a finite thickness of the trailing edge. We will discuss these two measures subsequently.

In Fig. 7.20 we show two generic trailing edges. The first trailing edge has a finite angle, while the upper and lower surface of the second trailing edge are parallel at point a. In the theoretical analysis of incompressible, inviscid flow the Kutta condition is applicable (see for example Ref. [3]). This simply implies that the flow smoothly leaves the trailing edge. If we apply this condition to the trailing edge with finite angle, we see that it can only be satisfied for the upper and lower surface when the velocities there are zero. This implies a stagnation point ($C_p = 1$) located at point a. If we consider the cusped trailing edge, we notice that the Kutta condition can be satisfied while the upper and lower velocity are larger than zero $C_p < 1$.

The only condition that applies is that upper and lower velocity are equal. This implies that $C_p < 1$ for a cusp trailing edge.

In practice we do not have inviscid conditions, and the presence of the boundary layer allows trailing-edge pressure coefficients to be lower than 1 (as is shown in many of the figures in this chapter). However, we still see that airfoils with cusped trailing edges allow for lower trailing edge pressure coefficients without separation than airfoils with a finite trailing-edge angle. Therefore, cusped trailing edges have a smaller adverse pressure gradient over the aft part of the airfoil, which postpones separation. Many supercritical airfoils therefore employ cusped trailing edges (e.g. SC(2)-0412 and DSMA-523a that have featured in this chapter).

One of the major disadvantages of having a cusped trailing edge is the lack of physical space in the trailing edge to make a structure. In this region of the wing often flaps or ailerons are positioned. Due to the diminishing trailing edge thickness, the second moment of area is relatively small. To give the trailing edge its required stiffness (to prevent aeroelastic deformation) a relatively heavy structure is required. Obviously, this introduces weight penalties, which eventually translate into an increase in induced drag (see Problem 7.6). To remedy this problem, aerodynamicists investigated the effect of cusped trailing edges with a finite thickness. It was shown that blunt trailing edges reduce the adverse pressure gradient on the upper surface by utilizing off-surface pressure recovery [41]. In practice this means that the pressure coefficient of the lower surface could be lower than the pressure coefficient on the upper surface.

Let us try to imagine what the effect of such a blunt trailing edge would be. First of all, we foresee an increase in base drag: the low pressure a the trailing edge acts on an aft-facing surface creating additional pressure drag. In subsonic conditions we therefore expect an increase in drag coefficient for a given lift coefficient (hence, a reduction of the lift-to-drag ratio). However, with increasing Mach number and the formation of a shock wave, the boundary layer is exposed to an ever increasing adverse pressure gradient. Due to the lower adverse pressure gradient of the airfoil with blunt trailing edge, the momentum thickness will be smaller (see also Example 6.4) reducing the total momentum loss in the boundary layer. So we have two effects at transonic conditions: an increase in pressure drag due to the blunt base of the airfoil, and a decrease in pressure drag due to the reduced momentum thickness at the trailing edge. Which of these two phenomena dominates depends on the relative thickness of the trailing edge compared to the airfoil chord. Investigations at NASA showed that the optimum trailing-edge thickness varied with the maximum thickness of the airfoil and was somewhat below 0.7 %c [17]. Figure 7.21 shows the effect of a blunt trailing edge on the drag coefficient development of an 11 % thick supercritical airfoil at $c_l = 0.7$. It becomes clear from this figure that at subsonic conditions the drag coefficient due to the blunt trailing edge is higher, while at transonic conditions (between $M = 0.68$ and $M = 0.79$) the blunt trailing edge reduces the drag coefficient.

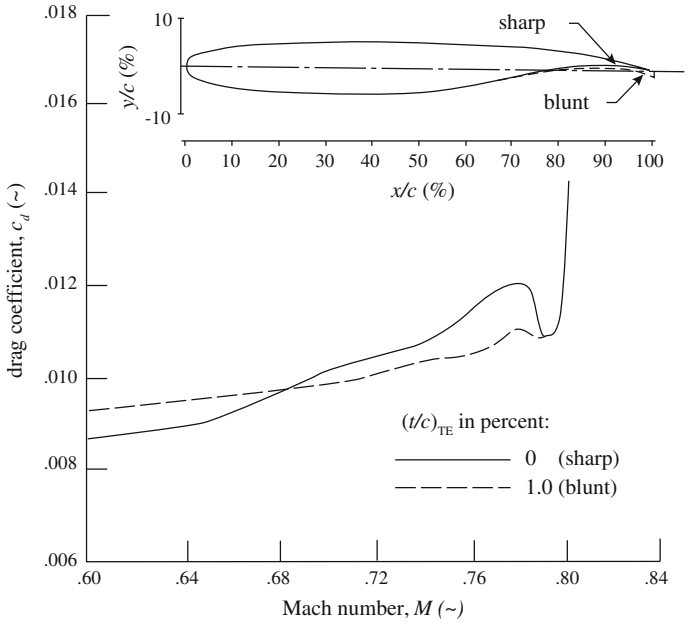

Fig. 7.21 Effect of blunt trailing edge on drag coefficient for an 11 % thick airfoil at $c_l = 0.7$ (after Ref. [17])

7.5 Low-Speed Stall

When an aircraft goes into a stall, the flow over the wing starts to separate from the upper wing surface and creates a wake of turbulent air. With increasing angle of attack this separated region becomes larger and larger, which reduces the rate at which lift increases. At a particular angle of attack, the rate at which the lift rises with angle of attack ($\mathrm{d}L/\mathrm{d}\alpha$) reduces to zero. At this point the aircraft experiences its maximum lift coefficient ($C_{L_{\max}}$). Increasing the angle of attack even further reduces the total lift of the airplane. At the same time, the wake becomes larger, which increases the drag. As the lift over the wing decreases, the moment balance on the aircraft is disturbed. Many aircraft are designed such that the horizontal tailplane provides a large enough nose down pitching moment to reduce the angle of attack once the wing stalls. During this motion the airplane starts to lose altitude and increases speed. While the angle-of-attack decreases, the flow remains separated. At an angle of attack well below the stall onset angle-of-attack the flow finally re-attaches to the wing and the airplane recovers from the stall. The latter effect is called stall hysteresis. This behavior is graphically shown in Fig. 7.22. We see the hysteresis effect on both the lift coefficient (Fig. 7.22a) and pitching moment coefficient (Fig. 7.22b).

The maximum (trimmed) lift coefficient is an important parameter for airplane performance. It is directly related to the required take-off field length and the landing

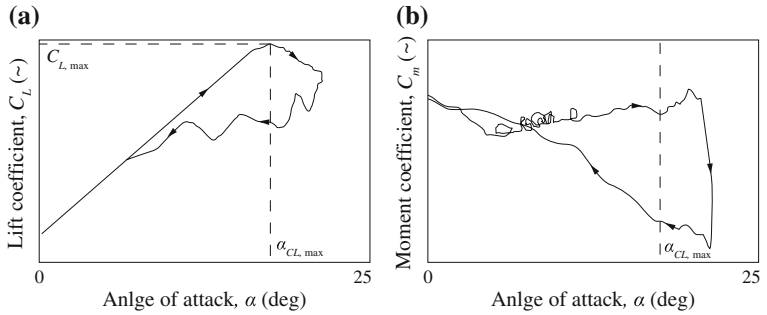

Fig. 7.22 Typical stall behavior of a passenger aircraft during flight. Data obtained from Ref. [12] for a Dornier 328. **a** Lift coefficient. **b** Moment coefficient

length of the aircraft. Therefore, many aircraft employ high-lift devices to increase the lift coefficient of the wing such that they can have a lower stall speed and therefore meet field length requirements. Typical high-lift devices are slotted flaps at the trailing edge and flaps, slats, or drooped noses at the leading edge. Fighter aircraft also employ their high-lift devices during combat maneuvers, which often occur in the transonic speed realm. At any lift coefficient the high-lift devices are automatically positioned such that maximum lift-to-drag ratio is achieved. This is an important parameter for the minimum turn radius or maximum turn rate that can be achieved.

Back to the maximum lift coefficient at low speeds and why it is important to treat this in a text on transonic aerodynamics. In the following subsections we discuss the various types of stall and the effect of Reynolds number and Mach number on the maximum lift coefficient of an airfoil. Furthermore, we present the aerodynamics of high-lift devices. We also show that transonic effects can often be the limiting factor for the maximum lift coefficient that can be achieved, even at low subsonic speeds.

7.5.1 Qualification of Low-Speed Stall

The mechanism of stall is universal in all cases. Be it low-speed or high-speed, stall is always caused by a separated boundary layer. To find out why a boundary layer separates it is instructive to review the reverse effect: attached flow. We know that at small angles of attack a fluid tends to nicely follow the contour of an airfoil. But why is this familiar concept so straightforward?

The tendency of a fast moving fluid to be attracted to a nearby surface is called the Coandă effect. It was named the effect after Henri Coandă. Coandă had become interested in the phenomenon after identifying that hot turbine air was attracted to nearby surfaces. The Coandă effect is a result of fluid entrainment. This means that when a jet of air moves in ambient air the low pressure of the jet pulls ambient air inwards towards the jet. When a nearby wall obstructs the surrounding fluid to be

pulled inwards, the jet moves to the body instead. Gasses experience the same effect around an airfoil. The flow is accelerated due to the presence of the body. Its pressure reduces (Bernoulli) and the flow 'sticks' to the body. The further away from the body, the lower the velocity increase. This principle has been illustrated in Sect. 6.2.1. The fact that the flow attaches to the body can therefore be attributed to the lower pressure of the fluid around it. When this pressure rises due to an adverse pressure gradient in the streamwise direction, the velocity of the air around the airfoil decreases and the Coandă effect diminishes. At the same time, the boundary-layer momentum reduces and reverse flow within the boundary layer marks the beginning of boundary layer separation (Chap. 6). When the angle of attack increases further, the boundary layer separates from the surface and becomes a shear layer between a turbulent wake and the laminar outer flow: the wing has stalled.

We distinguish three types of stall: leading-edge stall, trailing-edge stall, and thin-airfoil stall. The latter one is merely an artifact of low-Reynolds number flows and, contrary to what its name suggests, not only pertains to thin airfoils. At a certain angle of attack the laminar boundary layer separates due to the high adverse pressure gradient right after the nose of the airfoil. Further downstream the laminar boundary layer transitions to a turbulent boundary layer and re-attaches to the surface. The bubble of reverse flow that is formed between the separation and re-attachment point is called the laminar separation bubble. When increasing the angle of attack, this bubble expands downstream. Beyond a certain angle of attack the boundary layer does not reattach and a turbulent wake is present over the entire aircraft. This means an instant loss in lift and a large increase in drag. Most aircraft that are designed for high-subsonic speeds actually fly at higher Reynolds numbers, making thin-airfoil stall almost never seen in practice. However, scaled versions of these aircraft which are tested in at a lower Reynolds number in the wind tunnel could develop thin-airfoil stall. Thin-airfoil stall can be prevented by forcing transition to occur prior to the point where the boundary-layer separates from the surface.

Leading-edge stall occurs when the boundary layer is not capable of negotiating the large adverse pressure gradient that follows the suction peak on the nose. Before the stall angle of attack is reached as small laminar separation bubble forms just aft of the suction peak. This bubble may span as little as 1 % of the chord length and forms behind the suction peak under the steep adverse pressure gradient. The separated laminar boundary layer transitions over the bubble to turbulent and reattaches. Increasing the angle of attack moves this bubble forward and shortens it until the laminar boundary layer is incapable of reattachment. The result is that flow separates and that a wake is created starting at the nose of the airfoil (see also Fig. 6.23b). Alternatively, when a turbulent boundary layer is capable of reattachment it could still separate at a short distance behind the bubble due to the adverse pressure gradient. When either of these two events happens the suction peak over the leading edge collapses and a relatively constant pressure coefficient over the airfoil surface results. In the lift curve of the airfoil we see a step decrease in lift over a very small increment in angle of attack. A wake over the entire airfoil is created which creates a sudden increase in drag. In Fig. 7.23 leading-edge stall is shown for a 10 %-thick airfoil.

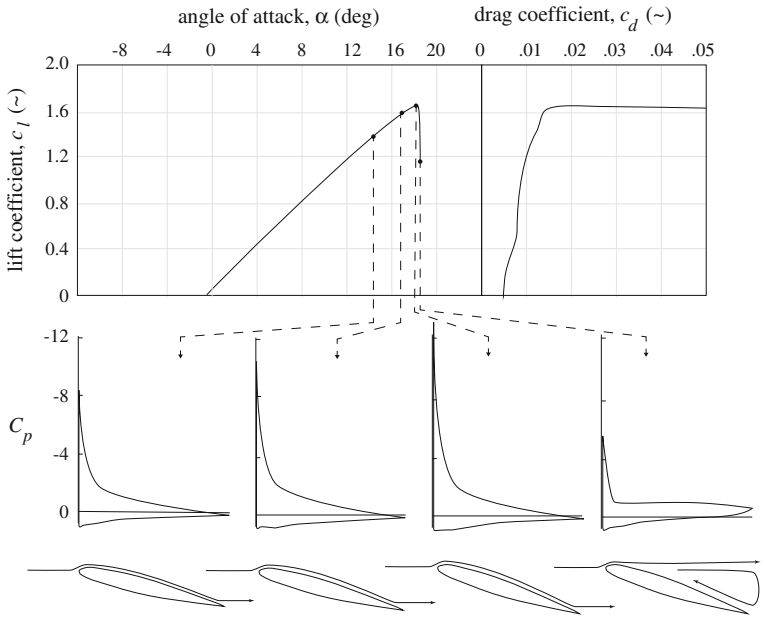

Fig. 7.23 Leading edge stall: notional lift and drag *curves* (*top*), typical pressure distributions (*middle*), and upper-surface stream line (*bottom*). Data based on Ref. [28] for Re $= 4.0 \times 10^6$, $M = 0.17$

Trailing-edge stall, on the other hand, is more gradual. Once the boundary layer has survived the steep adverse pressure gradient behind the leading edge, it progressively grows thicker and gets a higher shape factor. This means that the momentum of the boundary layer close to the wall is diminishing. At a certain angle of attack the boundary layer starts to separate at the trailing edge (usually when H is between 2.4 and 2.6), creating a small wake. Increasing the angle of attack further increases the adverse pressure gradient over the aft part of the airfoil and moves the separation point upstream. At the same time a laminar separation bubble could occur closer to the leading edge of the airfoil. With increasing angle of attack the size of the wake from the rear separation point increases and the pressure coefficient behind the separation point remains relatively constant. Increasing the angle of attack even further could merge the two separated regions creating a complete wake over the airfoil. Figure 7.24 visualizes the interaction between separation, pressure distribution and lift coefficient.

In the previous discussion we have treated leading-edge and trailing edge stall as if they were two independent types of stall. In practice often mixed types of stall occur. In such cases a short laminar separation bubble occurs after which the boundary layer reattaches. Further downstream the turbulent boundary layer separates indicating trailing-edge stall. The laminar separation near the leading edge can have a profound effect on the thickness of the boundary layer as is noted in [30]. The increase in the

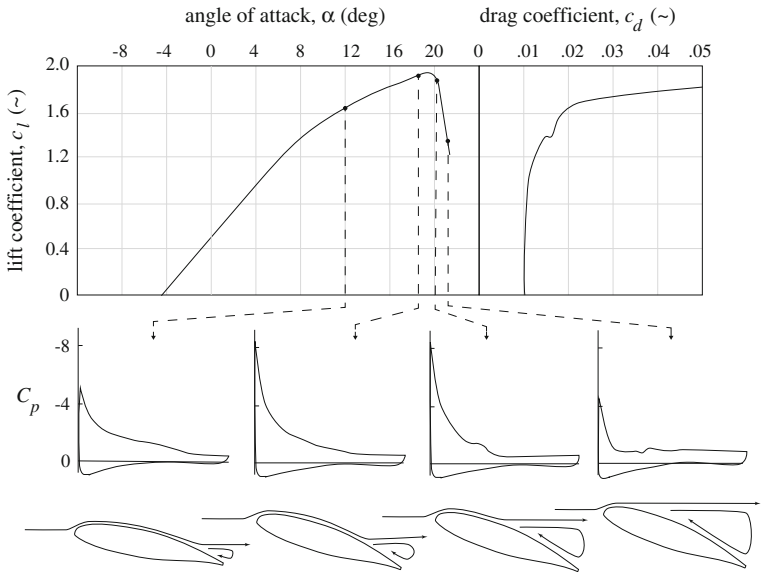

Fig. 7.24 Trailing edge stall: notional lift and drag *curves* (*top*), typical pressure distributions (*middle*), and upper-surface stream line (*bottom*). Data based on Ref. [31] for Re $= 6.3 \times 10^6$, $M = 0.15$

extent of an existing bubble increases the initial thickness of the turbulent boundary layer and, therefore, increases the tendency for the latter to separate. In this way the laminar separation bubble promotes the onset of turbulent stall near the trailing edge.

If we compare Figs. 7.23 and 7.24 we see that the difference in stall behavior is a function of the airfoil shape. Important parameters that determine whether leading or trailing-edge stall occurs include the thickness-to-chord ratio, the leading-edge radius, and the leading-edge camber. Typically, blunt and thick airfoils are more likely to suffer from trailing-edge stall, while sharp and thin airfoils suffer from leading-edge stall. In addition, the Reynolds number plays an important role whether the leading-edge or trailing-edge stall prevails.

7.5.2 Reynolds Effect on Maximum Lift Coefficient

With increasing wing size and flight speed, the Reynolds number grows. With increasing Reynolds number the (turbulent) boundary layer at a given location on the airfoil reduces in thickness according to (6.58). In general, increasing the Reynolds number increases the maximum lift coefficient for a given type of stall (leading-edge or trailing-edge). The thinner boundary layer is capable of negotiating a larger adverse pressure gradient without separating. There is, however, a more important Reynolds

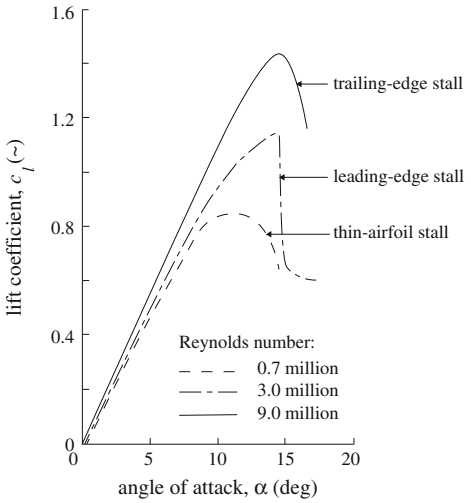

Fig. 7.25 Stall *curves* for a NACA 64_1-012 airfoil at various angles of attack (after Ref. [6])

number effect that is instrumental for the maximum lift coefficient: the position of the transition region. An increase in Reynolds number could also imply a switch from leading-edge stall to trailing-edge stall. In Fig. 7.25 this is demonstrated for a moderately thick airfoil, which' stall behavior is evaluated at three different Reynolds numbers. Note that this airfoil shows thin-airfoil stall at low Reynolds numbers even though it is not considered a thin airfoil. This confirms that thin-airfoil stall is not limited to thin airfoils. We explain the various Reynolds-number-related effects on stall in the subsequent paragraphs.

As the Reynolds number increases the position where the boundary layer transitions from laminar to turbulent shifts forward (see Sect. 6.5.4). As the region of transition has a large effect on the boundary layer development over the airfoil it has an impact on when (at what angle of attack) and where (right after re-attachment or at the trailing edge) the turbulent boundary layer separates. For a low Reynolds number the transition point lies downstream of the suction peak. If a small laminar separation bubble is present the boundary layer transitions from laminar to turbulent over the bubble and reattaches. The reattached boundary layer at the end of the separation bubble has a significantly higher thickness, which still grows in thickness downstream of the reattachment point. Increasing the Reynolds number shifts the transition region forward, which reduces the size of the separation bubble and consequently reduces the thickness of the boundary layer downstream of the bubble. The downstream boundary layer therefore separates at a higher angle of attack, which increases the maximum lift coefficient. When the transition region moves in front of the separation point, the effect of a higher Reynolds number is limited to the thickness decrease of the turbulent boundary layer, which could increase the maximum lift coefficient even further.

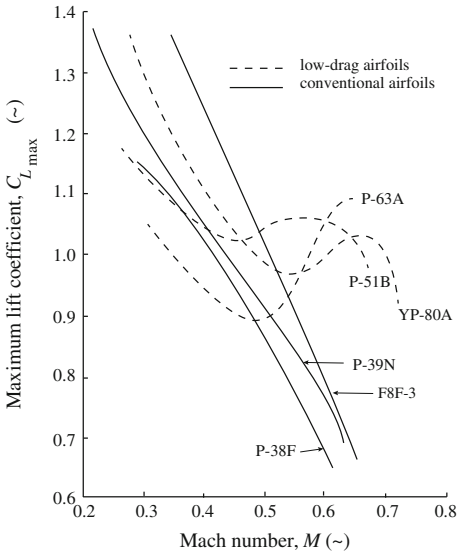

Fig. 7.26 Effect of Mach number on airplane maximum lift coefficient of several propeller aircraft (after Ref. [40]). *Note* data not at constant Reynolds number

7.5.3 Mach Effect on Maximum Lift Coefficient

The Mach number can have a significant effect on the maximum lift coefficient that can be attained. Even at low-subsonic conditions this statement holds up. In Ref. [40] it is shown through a series of flight tests how the airplane maximum lift coefficient is affected both by Reynolds and by Mach number. In Fig. 7.26 the maximum lift coefficients of six different propeller-powered aircraft are graphed as a function of the Mach number. Three aircraft used modified airfoils designed to promote a laminar boundary layer over a large part of the upper surface during cruise conditions (the 'low-drag airfoils'). The other three aircraft relied on NACA 4 and 5 series airfoils (the 'conventional airfoils'). We see a distinctly different maximum lift behavior between the airplanes having low-drag airfoils and the airplanes having the conventional airfoils. In the subcritical domain the uniform lowering of the maximum lift coefficient is attributed to the steepened adverse pressure gradient resulting from compressibility effects.

At Mach numbers beyond the critical Mach number the maximum lift coefficient is governed by the suction peak. In Fig. 7.27 it can be seen that increasing the Mach number reduces the suction peak for both types of airfoils. In both cases we see that the suction peak is widening with increasing Mach number. Furthermore, the low-drag airfoil develops a shock wave beyond $M = 0.63$. The pressure coefficient in front of the shock remains below the dash-dotted line, which corresponds to a maximum local Mach number. The minimum pressure coefficient always appears to stay below the dashed line, which also corresponds to a maximum local Mach number. We shall investigate why this happens.

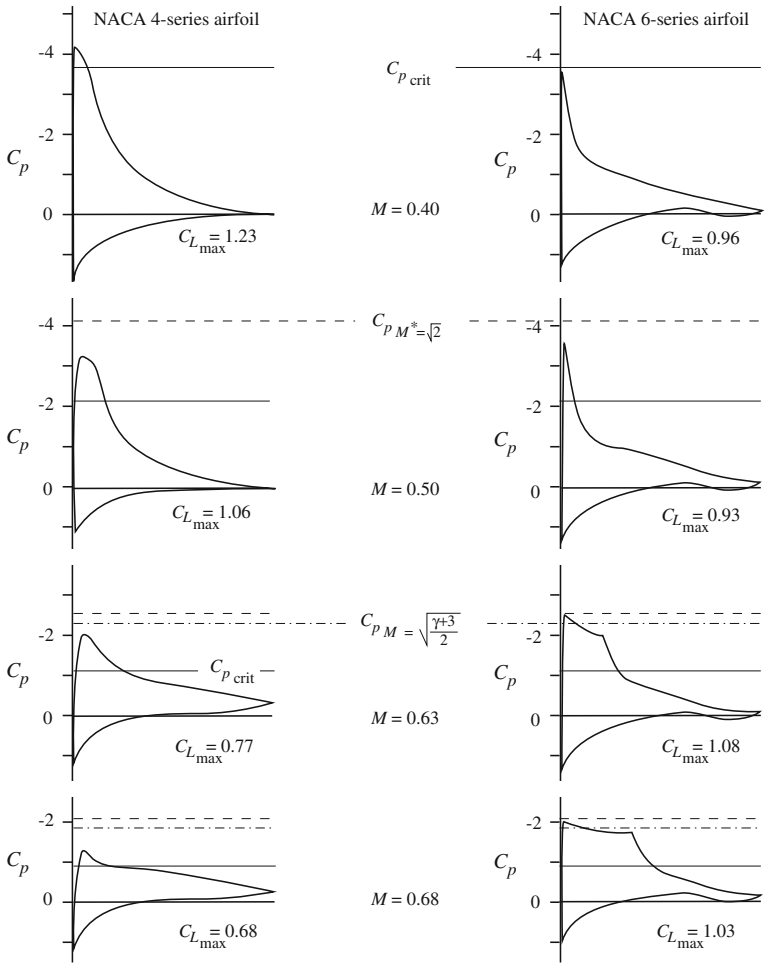

Fig. 7.27 Typical pressure distributions about NACA 4-series airfoils (*left*) and NACA 6-series airfoils (*right*) at maximum lift coefficient (after Ref. [40])

The same theoretical boundary has been shown in Fig. 6.9 where the dashed line shows a theoretical limit in local Mach number for supersonic flow over a convex surface embedded within subsonic flow. It has been shown that a characteristic Mach number of $M^* = \sqrt{2}$ is the highest Mach number for which Mach waves can exist for which the curvature is monotonic.[7] This corresponds to a situation where the streamline curvature is still continuous and the flow is isentropic and

[7] A monotonic curvature means that the Mach wave is either entirely convex or entirely concave. If Mach wave curvature is not monotonic it means an inflection point is present somewhere on the Mach wave.

uniform [27]. Via Eq. (4.10b) we calculate that this corresponds to a maximum local Mach number of:

$$M = \frac{2}{\sqrt{3-\gamma}} \approx 1.58 \quad \text{for} \quad \gamma = 1.4 \tag{7.5}$$

We can compare this maximum Mach number to the maximum Mach number that can be achieved in the throat of a supersonic convergent-divergent channel. In that case the flow is said to be choked. Whatever we do upstream or downstream of the throat, the Mach number can never exceed $M = 1$. In our case we have a similar condition only this time we consider external flow and limit the freestream Mach number to values below unity. The theoretical value of 1.58 is limited to flow over convex surfaces that provide monotonic curvature to the Mach waves. The absolute maximum is attained when discontinuities in streamline curvature are allowed. In this case the first discontinuity in streamline curvature starts at $M^* = \sqrt{2}$. This corresponds to theoretical accelerations of infinity at the point of discontinuity. The theoretical maximum that can be attained is referred to as the Ringleb solution [36]:

$$M = \frac{4}{3-\gamma} \approx 2.50 \tag{7.6}$$

For practical cases (7.5) is "the most likely maximum value to be approached in most cases," according to Laitone [24]. Substituting (7.5) in (6.17) and rewriting this for C_p yields a theoretical minimum local pressure coefficient as a function of the freestream Mach number:

$$C_{p_{M^*=\sqrt{2}}} = \frac{2}{\gamma M_\infty}\left[\left[\left(\frac{3-\gamma}{\gamma+1}\right)\left(1+\frac{\gamma-1}{2}M_\infty^2\right)\right]^{\frac{\gamma}{\gamma-1}} - 1\right] \tag{7.7}$$

This minimum has been indicated in Fig. 7.27 with the dashed line. Note that the minimum pressure comes very close to this value but never exceeds it. This confirms the statement that (7.7) is a practical limit on the minimum pressure coefficient and that (7.5) is a limiting Mach number. This analysis also demonstrates that even at speeds well below the speed of sound, transonic effects dictate maximum lift coefficient.

The theoretically obtained minimum pressure coefficient has been compared to experimental data obtained from a series of wind tunnel tests by Axelson [5]. As can be seen in Fig. 7.28 at Mach numbers beyond 0.5, considerably lower pressure coefficients can be obtained than those predicted by (7.7). An alternative prediction by Mayer comes closer to the measured values. Mayer based his predictions on a series of wind tunnel tests between $M = 0.4$ and $M = 2.2$ [29]. He proposed a statistical relation between the minimum value of the pressure coefficient and the freestream Mach number:

$$C_{p_{\min}} = \frac{-1}{M_\infty^2} \tag{7.8}$$

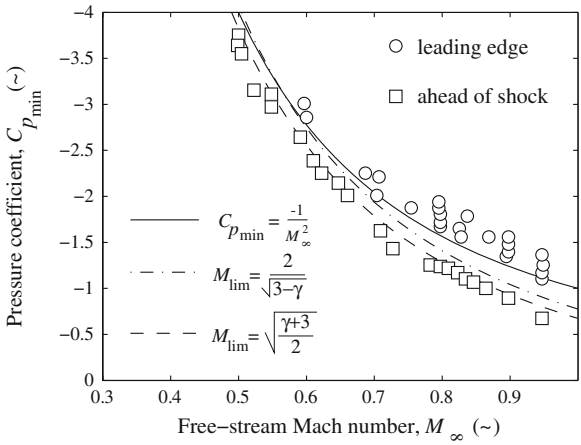

Fig. 7.28 Minimum pressure coefficients in transonic flow (after Ref. [5])

It can be shown (see Problem 7.9) that this results in a static pressure ratio of approximately 0.30 between the suction peak and the free stream. In other words, it is predicted to achieve 70 % of pure vacuum under the suction peak. At Mach numbers higher than 0.5 it can be seen from Fig. 7.28 that Mayer's prediction comes closer to the measured values published in [5], but still underestimates in certain cases.

If we return to Fig. 7.27 we observe that at $M = 0.63$ and $M = 0.68$, a shock wave is present for the low-drag airfoil. In addition, the dash-dotted line indicates a theoretical maximum local Mach number that cannot be exceeded in front of a shock wave without creating separated flow [24]:

$$M = \sqrt{\frac{\gamma + 3}{2}} \approx 1.48 \quad \text{for} \quad \gamma = 1.4 \tag{7.9}$$

In Ref. [24] it is demonstrated that for constant stagnation conditions ahead of the shock and a Mach number of 1.48 the maximum absolute value of p_2 (static pressure behind the shock) is achieved. In other words, for this limiting Mach number the maximum magnitude of static pressure recovery is achieved (although this is usually less than the free stream static pressure). If we imagine the local velocity to increase beyond this Mach number and form a shock wave further downstream, the static pressure recovery would be less (p_2 would be lower). Therefore, the higher subsonic free stream static pressure would push the normal shock wave back upstream until the maximum absolute static pressure would be produced. Substituting (7.9) in (6.17) and rewriting this for C_p yields a theoretical limiting local pressure coefficient in front of the normal shock wave:

$$C_{p_{M=\sqrt{\frac{\gamma+3}{2}}}} = \frac{2}{\gamma M_\infty^2} \left[\left[\left(\frac{2}{\gamma + 1} \right)^2 \left(1 + \frac{\gamma - 1}{2} M_\infty^2 \right) \right]^{\frac{\gamma}{\gamma-1}} - 1 \right] \tag{7.10}$$

This is confirmed by the graphs for $M = 0.63$ and $M = 0.68$ for the NACA 6-series airfoil in Fig. 7.27. We observe that the pressure coefficient is increasing between the suction peak and the shock. This indicates that the local Mach number is reducing from a value close to 1.58 to a lower value in front of the shock.

It is demonstrated in [11] that $M = \sqrt{(\gamma + 3)/2}$ is the only Mach number for which a curved streamline can become straight when passing through a normal shock wave. Consequently, it would be the most likely Mach number in front of a shock wave whenever boundary layer separation occurs at the foot of the shock. If we combine these observations we can conclude that on convex profiles the maximum Mach number in front of a normal shock wave never exceeds 1.48 and that it is likely that this shock causes boundary layer separation. Evidence of the accuracy of this predicted pressure coefficient is presented in Fig. 7.28. The experimental data consistently shows that the value of $M = 1.48$ ahead of the shock is never exceeded in any of the experimental tests.

7.5.4 High-Lift Devices

Most high-subsonic aircraft have leading-edge and trailing-edge devices to allow for a higher lift coefficient and hence a lower stall speed. Many contemporary aircraft use slats or leading-edge flaps to increase the stall angle of attack, while trailing-edge flaps are used to increase the camber of the wing and extend the local chord. The combined effect can increase the maximum lift coefficient by more than 100 %. The reader is referred to [33] or [38] for a general discussion on the aerodynamics of high-lift devices. In this section we limit ourselves to the transonic effects that accompany the flow over multi-element airfoils.

The idea behind high-lift devices is to increase the maximum lift coefficient. This can only be achieved if the suction over the upper surface is magnified without boundary layer separation. The slots between the individual components play a pivotal role to achieve this [38]. However, the same aerodynamic limitations in terms of Reynolds and Mach number effects, as discussed previously, exist for multi-element airfoils. Increasing the Reynolds number has a beneficial effect on the maximum lift coefficient, while the maximum local Mach number limits the minimum pressure coefficient and therefore the lift coefficient. The main difference with single-element airfoils is the magnitude of the suction peak. For well-designed multi-element airfoils, the highest suction peak occurs on the slat and can easily exceed $C_p = -20$ at a theoretical Mach number of zero. As we now know, the transonic effects therefore occur at much lower freestream conditions sometimes as low as $M = 0.2$. This means that the stall speed of an aircraft in landing configuration at sea level, V_{s0}, could in fact be limited by the maximum supersonic Mach number over the leading edge of the slat (see Problem 7.10).

Figure 7.29 shows the airfoil of the A320 wing in landing configuration with slat and flap deployed. The dash-dotted lines indicate the edge of the various boundary layers that are formed on this multi-element airfoil. We can see how the wake of

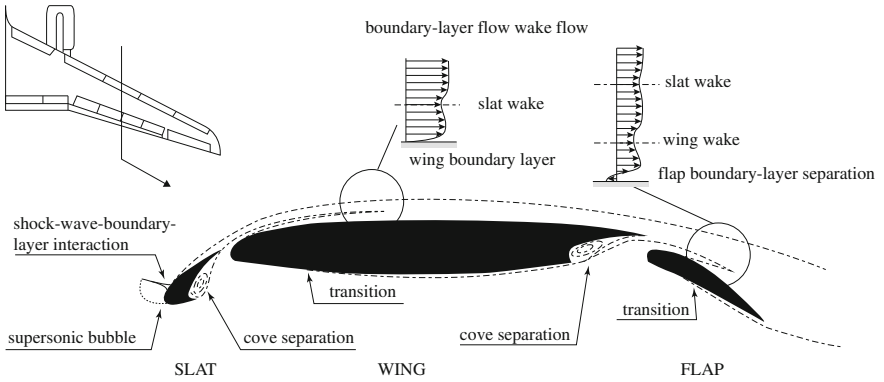

Fig. 7.29 A320 airfoil in landing configuration (modified from Ref. [13])

the slat merges with the boundary layer of the wing. This is termed *boundary layer confluence*. This happens again over the upper surface of the flap where the wake of the wing surface merges with the flap boundary layer. In this example, there exists reversed flow over the flap, which indicates the onset of stall. Over the slat we also observe a local bubble of supersonic flow that is terminated with a shock wave. Under the shock wave the flow transitions from laminar to turbulent resulting in a thickening of the boundary layer. We can imagine how, with increasing Mach number, the strength of the shock wave increases, which eventually results in boundary-layer separation at the shock foot (see also Sect. 7.6.1). It is this phenomenon that effectively limits the maximum lift coefficient as a function of the freestream Mach number.

To substantiate these claims, consider Fig. 7.30. Here we have a typical multi-element airfoil consisting of a slat and a double-slotted flap system. The graph shows the minimum pressure coefficients measured at the suction peak on the leading edge of the slat. In addition, the statistical limit by Mayer (7.8) as well as the theoretical limit of (7.7) are shown. Note that the theoretical limit predicts a lower pressure coefficient than the statistical prediction by Mayer on this low-subsonic domain. The symbols indicate various combinations of flap and slat deflection. We clearly see that the boundary is formed by the limiting Mach number of $M = 2/\sqrt{3-\gamma}$, regardless of the flap or slat setting. We also observe a decrement in minimum pressure coefficient before the local Mach number reaches the limiting value. In the cases where the slat is deployed the decrement in lift coefficient between $M_\infty = 0.19$ and $M_\infty = 0.28$ for this particular airfoil is between 0.3 and 0.4 [46]. This causes a 10 % decrease in maximum lift coefficient due to the transonic "choking" of the flow over the slat leading edge.

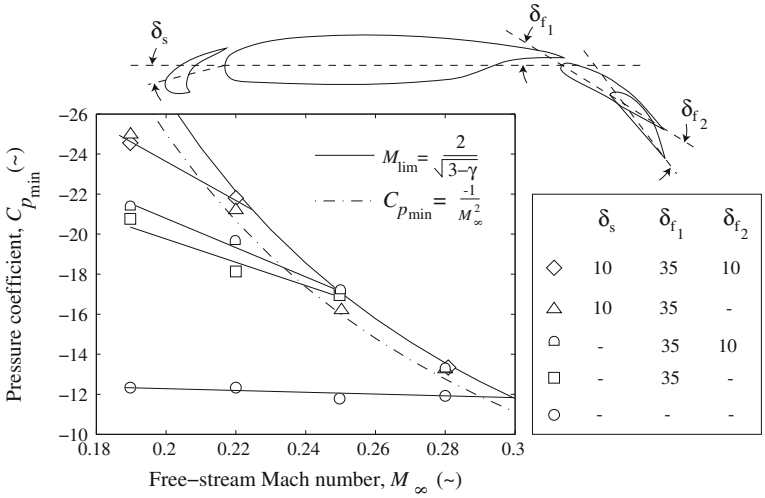

Fig. 7.30 Minimum pressure coefficients at the leading-edge suction peak for Re $= 6.9 \times 10^6$ (after Ref. [46])

7.6 High-Speed Stall

High-speed stall is often characterized by the onset of aerodynamically induced vibrations. In general, the term *buffet* is used for broadband vibrations induced by pressure fluctuations in the flow. In the present context *buffet* refers to transonic buffet. Transonic buffet is primarily caused by separation of the boundary layer that occurs at the foot of the shock wave [33]. Shock-induced vibrations are typical to high-subsonic commercial jet transports. There is a relatively weak aeroelastic interaction because the frequency of the shock-induced vibrations can be several orders of magnitude beyond the wing natural frequencies. However, buffet has a profound effect on the maximum lift capability of the wing at high (transonic) Mach numbers. Airworthiness regulations stipulate that there needs to be a margin of 30 % between the design-lift coefficient and the lift coefficient at which buffet onset occurs for any operating Mach number. This margin is defined by a 1.3 g maneuver or a vertical gust. In practice, this limits the cruise lift coefficient in the design condition. If we plot the buffet-onset lift coefficient against the Mach number we have the *buffet onset boundary*. Figure 7.31 schematically demonstrates the buffet onset boundary and the required margins in terms of ΔC_L and ΔM_∞.

The buffet-onset boundary presents limitations to the maximum lift coefficient of the airplane at each Mach number. With respect to our very simple Breguét equation (1.1), we see that ideally we would like to maximize the combination of M_∞ and C_L, while keeping the C_D as low as possible. Or, vice versa, reduce the fuel burn (and consequently the operational cost) for a given range. The buffet boundary of a given wing could therefore be a constraint on the commercial viability of an aircraft.

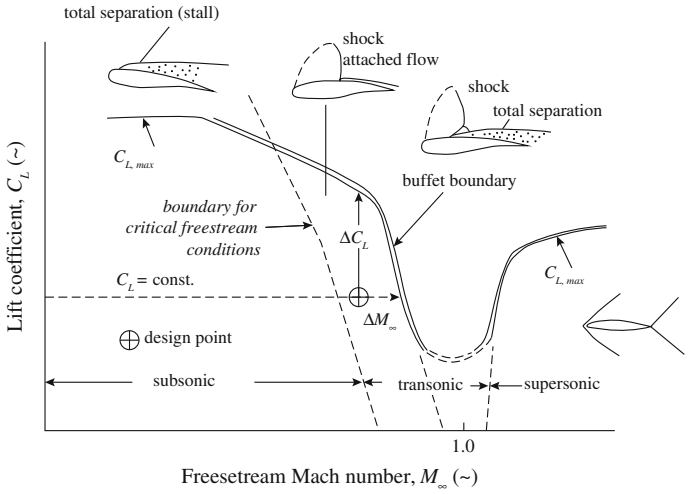

Fig. 7.31 Separation boundary at various Mach numbers and lift coefficients (after Ref. [42])

In addition, this combination of Mach number and lift coefficient effectively limits the altitude an airplane can reach at a given Mach number when flying in steady, symmetric, horizontal flight (see Problem 7.11).

7.6.1 Flow Separation at the Shock Foot

Transonic buffet is an off-design condition for high-subsonic aircraft. It occurs when the supervelocities over the top side of the airfoil become relatively large and the shock wave that terminates the supersonic domain increases in strength. Such large supervelocities can occur when the aircraft encounters a gust (i.e. an increase in freestream Mach number) or when it performs a maneuver and requires a higher lift coefficient. The mechanics of transonic buffet can entirely be related to the shock boundary layer interaction as discussed in Sect. 6.4.3. If we re-examine Fig. 6.40 we see the separation bubble under the shock. With increasing shock strength the size of this bubble increases until it merges with the small separated region close to the trailing edge.

The shock-induced separation was studied by Pearcey in the early 1950s [34]. He systematically investigated the effect of flow parameters such as incidence angle (or angle of attack) and freestream Mach number on the shock-induced separation. In Fig. 7.32 we see schlieren images of the flow about a 6% thick airfoil (RAE 104) under an angle of attack of 2°. In the schlieren image the density gradients in the flow are visualized. The shadow pattern is a light-intensity representation of the expansions (low density regions) and compressions (high density regions) which characterize the flow.

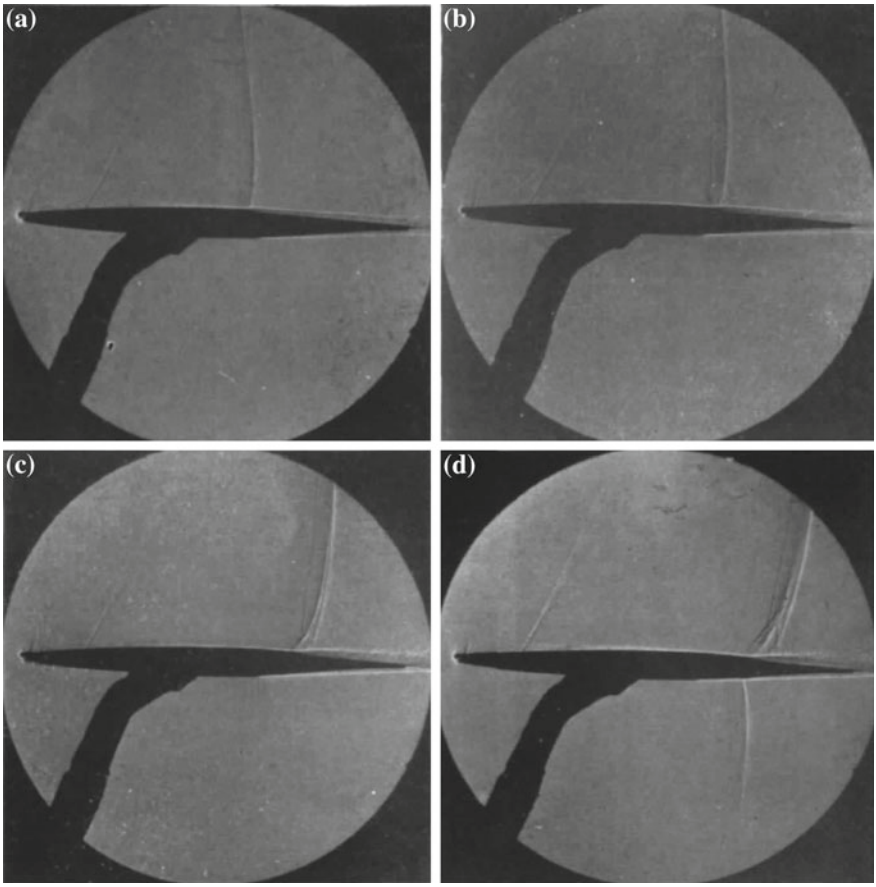

Fig. 7.32 Schlieren images of the flow around a 6 % thick RAE 104 airfoil at 2° angle of attack (from Ref. [34]). **a** $M = 0.84$. **b** $M = 0.86$. **c** $M = 0.88$. **d** $M = 0.90$

Let us progressively analyze the schlieren images in Fig. 7.32. At $M = 0.84$ we see an the shock wave located at around the 60 % chord. The boundary layer is still attached. At $M = 0.86$ the shock wave moves aft and its strength grows (the pressure ratio over the foot of the shock is beyond 1.4). A separation bubble under the shock occurs. However, the boundary layer remains attached and the trailing edge pressure is unaffected. Increasing the Mach number to $M = 0.88$ causes the boundary layer to fully separate from the shock foot. This decreases the trailing edge pressure substantially. Because the trailing edge pressure on the upper and lower surface are equal (assuming no off-surface pressure recovery), this also affects the development of the flow on the lower surface. The lower trailing edge pressure induces higher supervelocities on the lower surface. If the Mach number is increased to $M = 0.90$ we see that also on the lower surface a shock has formed. In addition, the severe separation

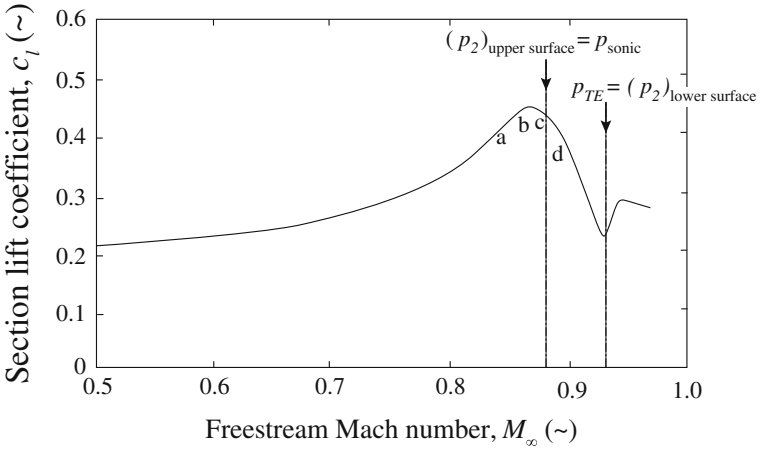

Fig. 7.33 Development of the section lift coefficient of the 6 % thick RAE 104 airfoil at $\alpha = 2$ (after Ref. [34]). *Note* p_2 indicates the pressure downstream of the shock, P_{TE} is the trailing edge pressure, while p_{sonic} corresponds to the pressure for sonic flow at points downstream of the shock, i.e. $p_{\text{sonic}} = 0.528 p_t$

on the upper surface creates an inclined ramp for the flow outside the boundary layer resulting in a more oblique shock wave terminating the supersonic domain.

The effect of shock-induced separation on the lift coefficient is shown in Fig. 7.33. The letters *a* through *d* refer to the respective images in Fig. 7.32. We see that the maximum lift coefficient at a constant angle of attack is reached around $M = 0.87$. When the boundary layer fully separates from the surface the lift coefficient starts to decrease rapidly. Most of this decrease is caused by the increase in suction over the lower surface due to the decrease in trailing-edge pressure when the boundary layer has separated. With increasing Mach number, the shock wave on the lower surface moves faster towards the trailing edge than the upper shock wave creating more suction over the lower surface and hence reducing the lift coefficient. A minimum is obtained when the lower shock reaches the trailing edge. Increasing the Mach number even further results in a higher value of the lift coefficient that corresponds with both shocks having reached the trailing edge.

In Fig. 7.34 we schematically repeat this development of the shock pattern over a generic airfoil of low thickness. The same effects as in the wind tunnel are seen as can be verified by comparison to Fig. 7.32. In Fig. 7.34 the strength of the shock has been indicated by the thickness of the shock line. Note how the shock strength is highest at the surface, while its strength decrease further away from the body. Intuitively, we can verify this because the supervelocities are highest close to the surface. Furthermore, the relative size of the shock wave increases with higher Mach number. At $M = 1.4$ the shocks at leading and trailing edge even exceed the bounds of this figure. Finally, the notional point of separation is shown along with the growth of the wake over the transonic regime. Note how the wake grows up to $M = 0.9$ and decreases again above that value.

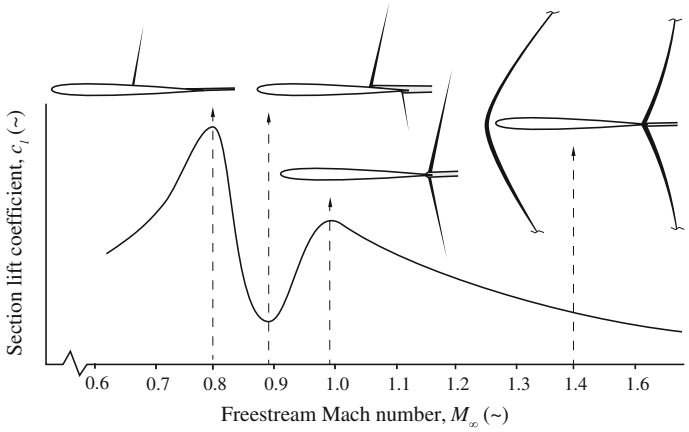

Fig. 7.34 Notional development of section lift coefficient over a symmetric airfoil at $\alpha = 2$

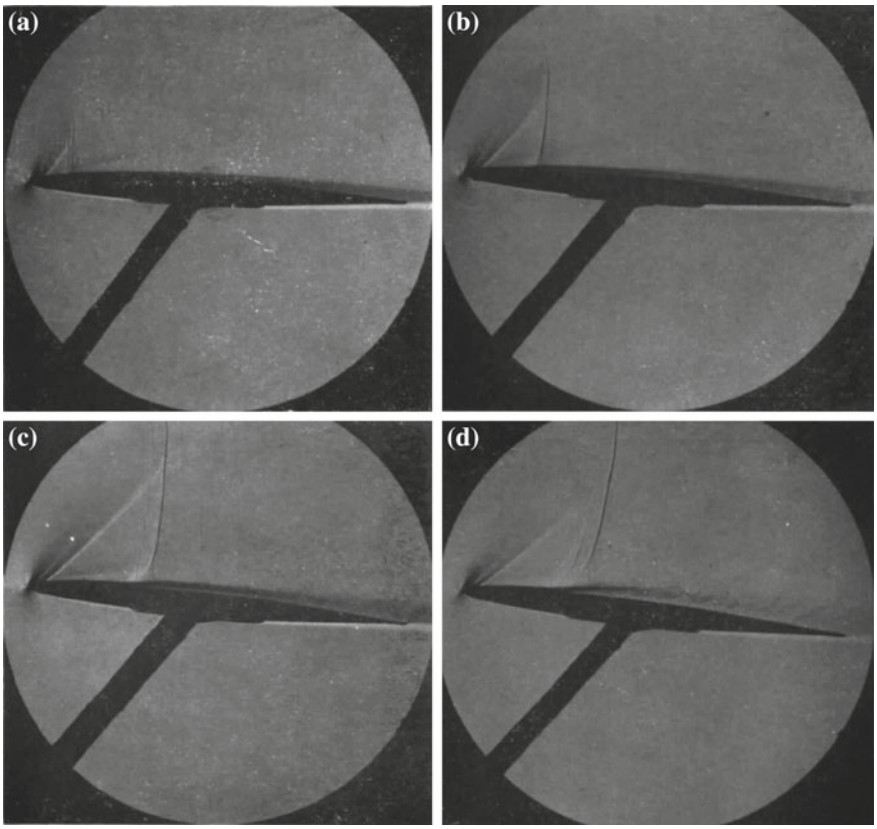

Fig. 7.35 Schlieren images of the flow around a 6 % thick RAE 104 airfoil at $M = 0.75$ (from Ref. [34]). **a** $\alpha = 2.7°$. **b** $\alpha = 3.7°$. **c** $\alpha = 4.7°$. **d** $\alpha = 5.7°$

Let us follow Pearcey [34] in his investigation into the behavior of shock-induced separation at constant Mach number and increasing angle of attack. In Fig. 7.35 we see schlieren images of the same airfoil as in Fig. 7.32. The Mach number has been fixed at $M = 0.75$ while the angle of attack increases progressively from $\alpha = 2.7°$ through $\alpha = 5.7°$. It is important to note that the transition has been artificially induced at the nose and that the shock wave interacts with a turbulent boundary layer at any of the aforementioned angles of attack. We see that somewhere between $\alpha = 2.7$ and $\alpha = 3.7$ the boundary starts to separate at the shock foot. The shock is still quite close to the leading edge and the boundary layer reattaches downstream. With increasing angle of attack the shock moves aft and the separation bubble expands rapidly towards the trailing edge. This causes the trailing edge pressure to decrease and the shock to halt before it starts to move forward. At even higher angles of attack the shock moves further forward together with the separation point.

In Fig. 7.36 the position of the shock foot is plotted for a range of angles of attack and Mach numbers. We distinguish uniform behavior at the various Mach numbers: initially the shock moves aft up to the point that the separation bubble reaches the trailing edge. Beyond that angle of attack the shock wave and the separation point move forward. With decreasing Mach number the angle of attack at which shock-induced separation starts becomes progressively higher. Simultaneously, the shock position at which separation starts becomes closer to the leading edge. It becomes difficult to judge at what Mach number the separation ceases to be induced by the shock instead of being induced by the adverse pressure gradient behind the suction peak, as seen at low speeds.

Let us take a look at the effect of shock-induced separation on the lift coefficient. In Fig. 7.37 we see the lift coefficient development over the RAE 104 airfoil at two Mach numbers. In 7.37a we see that lift coefficient remains close-to constant beyond the point where the separation bubble reaches the trailing edge. For $M = 0.80$ we expect the separation to start at a lower lift coefficient. This is indeed the case as can be seen in Fig. 7.37b. However, here we have somewhat of a different case.

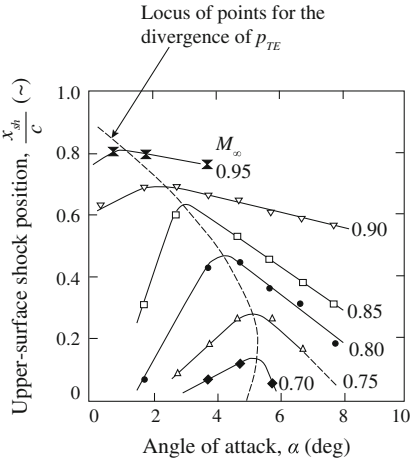

Fig. 7.36 Shock position as a function of angle of attack for a 6 % thick RAE 104 airfoil with fixed transition at the nose (after Ref. [34])

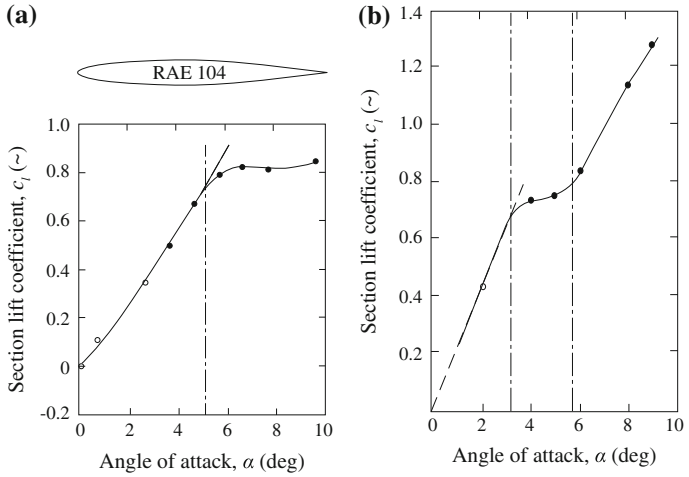

Fig. 7.37 Lift versus angle of attack for a 6 % thick RAE 104 airfoil at two transonic Mach numbers (after Ref. [34]). **a** $M = 0.70$. **b** $M = 0.80$

The lift coefficient increases even when the shock-induced separation covers the upper surface from shock foot to trailing edge. Such behavior is attributed to off-surface pressure recovery and occurs beyond the angle of attack where the pressure coefficient at the trailing edge falls below the critical pressure coefficient. When this is the case, the pressure coefficient at the trailing edge has no effect anymore on the development of the flow over the lower surface. With increasing angles of attack, the pressure coefficient on the lower surface begins to rise again. At the same time, the pressure coefficient on the upper surface decreases even further below the critical pressure coefficient allowing the shock wave to move backwards resulting in an increase in suction over the upper surface. The combined effect is an increase in lift coefficient beyond the angle of attack of shock-induced separation. This effect is dependent on the presence of off-surface pressure recovery and therefore partially on the shape of the airfoil trailing edge.

7.6.2 Transonic Buffet

In the previous section we have examined the effect of separation at the shock foot at transonic speeds. We know from experience with low speed stall that separation and the associated wake cause pressure fluctuations that are transmitted to the airfoil. These fluctuations in pressure can be felt as structural vibration. Apart from these fluctuations the separated flow is considered to be steady (e.g. invariant with time). In transonic conditions, however, the separated boundary layer can also cause a periodic motion of the shock wave over the surface of the airfoil. Such fluctuations usually have a frequency on order of 10^2 Hz and generate large fluctuations in pressure (see Fig. 7.38). These large fluctuations can be felt as a strong vibration in the airframe

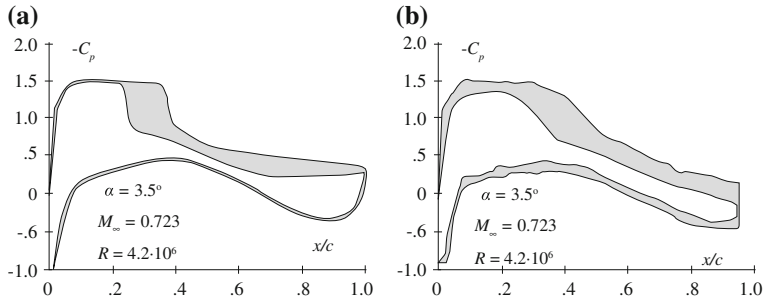

Fig. 7.38 RA16SC1 airfoil. Envelope of the pressure distributions at buffet onset (after Ref. [25]). **a** Calculation. **b** Experiment

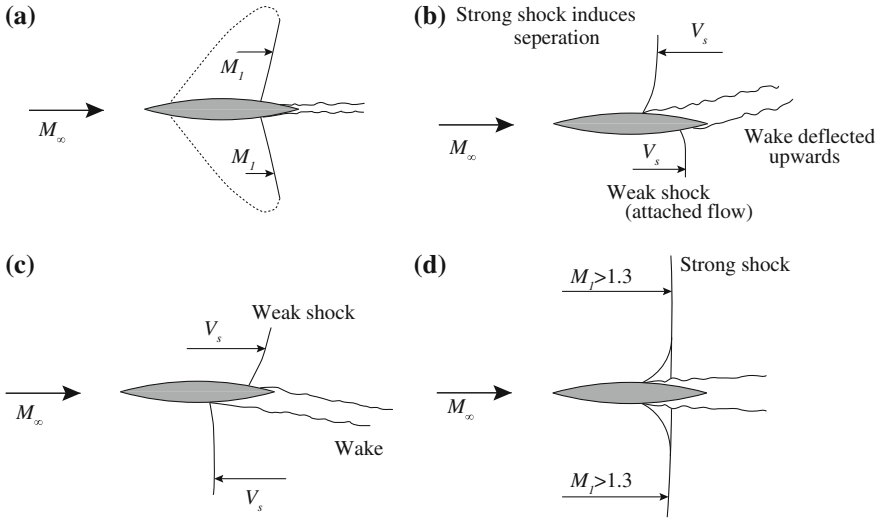

Fig. 7.39 Shock wave development over a 14 % thick circular arc airfoil with increasing subsonic freestream Mach number (after Ref. [14]). **a** $M_1 < 1.2$ (no separation). **b** $M_1 > 1.2$ start periodic flow. **c** 1/2 cycle after (**b**). **d** $M_1 > 1.3$ shock too strong for reattachment

structure. This phenomenon is termed transonic buffet and its mechanics is further explained in this section.

Before we look at a realistic case of transonic buffet on a supercritical airfoil it is instructive to consider the shock motion over a circular arc airfoil. The shock development over a 14 % thick circular arc airfoil at symmetric flow conditions is presented in Fig. 7.39. In Fig. 7.39a we see shocks of equal strength appearing at both the upper and lower surface. In Fig. 7.39b we assume that a pressure disturbance upstream of the shock on the upper surface causes the shock to move more forward. The instantaneous shock Mach number (M_s) is given by:

$$M_s = M_1 + \frac{1}{a}\frac{\mathrm{d}x_s}{\mathrm{d}t} \tag{7.11}$$

where x_s is the location of the shock and $\mathrm{d}x_s/\mathrm{d}t = V_s$ is the velocity of the shock wave with respect to the airfoil. As the shock moves forward M_s increases beyond the Mach number at which separation is triggered. So as the shock moves forward it also shifts the separation point forward creating an asymmetric wake. At the same time, the trailing edge pressure decreases which moves the shock on the lower surface closer to the trailing edge. In moving backward, M_s decreases which prevents the boundary layer from separating. As the upper shock moves forward over the convex surface it encounters a slower supersonic region. Therefore, its strength weakens as it moves upstream. The flow attaches at a point where the shock becomes too weak to initiate separation. On the lower side the reverse is happening. As the shock moves closer to the trailing edge its strength is increasing and at some point it initiates separation. This causes the wake to move to deflect downward as can be seen in Fig. 7.39c. This process is now repeating itself on the lower surface. The deflected wake essentially causes the shock on the lower surface to move forward, while the shock on the upper surface starts to move backward. Even though there is a time lag between the downward deflection of the wake and the motion of the shock wave, the flow can maintain a self-sustained periodic motion. Finally, when $M_1 > 1.3$ (Fig. 7.39d) the shock is strong enough at all times to cause separation. No reattachment can take place and the periodic motion of the shock wave ceases.

Close to the surface of the airfoil we can approximate the flow as one dimensional. We follow Ref. [26] to relate the oscillating shock position to the oscillating strength of the shock wave. The latter one is given as the ratio of static pressure over the shock wave. We denote the properties of the flow ahead of the shock wave with a subscript 1 and behind the shock with subscript 2. The shock strength would then be quantified as p_2/p_1. We assume that the flow has a varying velocity, u, a varying static pressure, p, and a varying speed of sound, a, in the streamwise (x) direction. The displacement of the shock in time is given by Δx. The pressure and velocity in front and behind the shock can be written as follows:

$$p_1 = P_1 + \frac{\mathrm{d}P_1}{\mathrm{d}x}\Delta x + \tilde{p}_1 \tag{7.12}$$

$$p_2 = P_2 + \tilde{p}_2 \tag{7.13}$$

$$u_1 = U_1 - u_s + \tilde{u}_1 + \frac{\mathrm{d}U_1}{\mathrm{d}x}\Delta x \tag{7.14}$$

$$u_2 = U_2 - u_s + \tilde{u}_2 \tag{7.15}$$

where $\tilde{p}$ and $\tilde{u}$ are perturbation pressures and velocities, respectively, and P and U are the steady-state pressures and velocities, respectively. We know that the pressure ratio over the shock wave is given by the Rankine-Hugoniot relation:

$$\frac{p_2}{p_1} = 1 + \frac{2\gamma}{\gamma+1}\left(\frac{u_1^2}{a_1^2} - 1\right) \tag{4.14}$$

Substitution of (7.14) yields a long expression of p_2/p_1 as a function of each of the velocity components in (7.14). We omit this expression for brevity. We assume that

the velocities of $\tilde{u}$, u_s, and $\frac{dU_1}{dx}\Delta x$ are an order of magnitude smaller than U_1. We therefore only retain the multiples of U_1 leading to the following expression:

$$\frac{p_2}{p_1} = 1 + \frac{2\gamma}{\gamma+1}\left[M_1^2 - 1 + 2M_1\left(\frac{\tilde{u}_1}{a_1} - \frac{u_s}{a_1} + \frac{dU_1}{dx}\frac{\Delta x}{a_1}\right)\right] \tag{7.16}$$

where we substituted $M_1 = U_1/a_1$. We identify the steady-state part of the Rankine-Hugoniot equation with an additional term between brackets encompassing the velocity terms introduced by the shock motion. We rewrite (7.16) therefore accordingly:

$$\frac{p_2}{p_1} = \frac{P_2}{P_1} + \frac{4\gamma}{\gamma+1}M_1\left(\frac{dM_1}{dx}\Delta x - \frac{u_s}{a_1} + \frac{\tilde{u}_1}{a_1}\right) \tag{7.17}$$

where P_2/P_1 can be obtained by employing (4.14) for $u_1 = U_1$. If we assume that the shock oscillates periodically over a distance Δx_0 we can write the shock displacement, velocity and perturbation quantities as follows:

$$\Delta x = \Delta x_0 e^{i\omega t}, \quad u_s = i\omega \Delta x_0 e^{i\omega t}, \quad \tilde{u}_1 = \bar{u}_1 e^{i\omega t} \tag{7.18}$$

where $\bar{u}_1$ is the time average of the perturbation velocities ahead of the shock. Substituting (7.18) in (7.17) yields an expression for the time dependency of the shock strength:

$$\frac{p_2}{p_1} = \frac{P_2}{P_1} + \frac{4\gamma}{\gamma+1}M_1\left(\frac{dM_1}{dx} - \frac{i\omega}{a_1} + \frac{\bar{u}_1}{a_1}\right)\Delta x_0 e^{i\omega t} \tag{7.19}$$

If we assume that the disturbances in the supersonic region upstream of the shock are negligible (i.e. $\tilde{u}_1 \approx 0$) the relation reduces to:

$$\frac{p_2}{p_1} = \frac{P_2}{P_1} + \frac{4\gamma}{\gamma+1}M_1\left(\frac{dM_1}{dx} - \frac{i\omega}{a_1}\right)\Delta x_0 e^{i\omega t} \tag{7.20}$$

Let us try to interpret the contents of (7.20). On the RHS it requires the input of the shock oscillation: amplitude (Δx_0) and frequency (ω in rad/s). In addition, it requires an estimate for the change in upstream Mach number with displacement (dM_1/dx) at the neutral position of the shock. Finally, it requires an estimate of the steady state properties of the shock: P_2/P_1 and M_1.

Example 7.3 Assume we have a NACA 64A006 airfoil at $M = 0.90$ which has an induced shock oscillation (this experiment is described in Ref. [43]). The steady-state Mach number in front of the shock has been determined from quasi-steady conditions and is $M_1 = 1.18$ and $dM_1/dx = 1.7$. A periodic shock motion is induced with a frequency of 120 Hz and an amplitude of $\Delta x_0/c = 0.05$. The static temperature in front of the shock wave is 290 K. Calculate the following:

(a) The steady-state pressure ratio, P_2/P_1
(b) The amplitude of the pressure ratio
(c) The phase shift in radians between pressure jump and shock position.

Solution:

To calculate the steady shock jump in static pressure we employ (4.14):

$$\frac{P_2}{P_1} = 1 + \frac{2\gamma}{\gamma+1}\left(M_1^2 - 1\right) = 1.46$$

This means that the time-averaged pressure ratio is 1.46 over this shock. To find the amplitude of the pressure ratio we employ part of (7.20):

$$\text{amplitude} = \frac{4\gamma}{\gamma+1} M_1 \sqrt{\left(\frac{\mathrm{d}M_1}{\mathrm{d}x}\right)^2 - \left(\frac{i\omega}{a_1}\right)^2}\, \Delta x_0 = 0.380$$

Finally, we determine the face shift between the shock position and the pressure jump. We plot one period for the shock position and pressure jump, respectively, in Fig. 7.40. We see that the pressure jump is lagging the shock position. We calculate the phase shift, φ, as follows:

$$\varphi = \tan^{-1}\left(\frac{\omega}{a_1}\frac{\mathrm{d}x}{\mathrm{d}M_1}\right) = 0.91 \text{ (rad)}$$

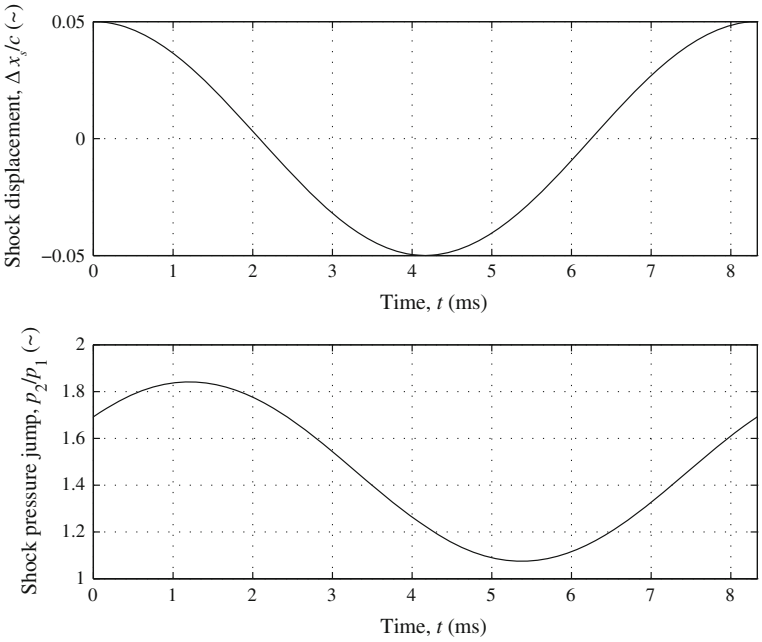

Fig. 7.40 Oscillating shock position and corresponding pressure jump according to (7.18) and (7.20), respectively

The phase shift between shock position and pressure jump amounts to 1.21 ms. For clarity, the oscillating shock position and oscillating shock jump are shown in Fig. 7.40.

In the previous example it becomes clear that the shock pressure jump periodically alters between $p_2/p_1 = 1.83$ and $p_2/p_1 = 1.09$. With the knowledge in mind that the pressure magnitude of the pressure jump is dominant for boundary layer separation, we can deduce from this simple example that when the shock is weakest it is conceivable that the boundary layer remains attached. Vice versa, it also conceivable that when the shock strength passes a certain threshold the boundary layer fully separates. Pearcey suggested separation to occur when $p_2/p_1 > 1.4$. The limiting Mach number of (7.9) predicts separation to occur at $p_2/p_1 = \gamma + 1$ (see Problem 7.13).

The shock motion in the previous example was induced by deflecting a control surface ($c_f = 0.25c$) with an amplitude of 1°. The deflection of the control surface caused an oscillation in the wake and an oscillation in the back pressure of the shock wave. When separated and attached flow follow each other rapidly we see similar behavior: an oscillating wake causing an oscillating shock wave (see also Fig. 7.39). The amplitude and phase shift of the pressure jump are largely dependent on the sensitivity of the upstream Mach number (M_s) to the shock position as well as on the frequency, f. It can be shown (see Problem 7.14) that when $\mathrm{d}M_1/\mathrm{d}x \to 0$ the phase shift tends to $\pi/2$ or 90°. Furthermore, when the frequency increases the amplitude of the shock decreases as is demonstrated in Ref. [43]. This results in a frequency at which the amplitude of the static pressure jump is maximum (see Problem 7.15).

Example 7.4 One of the prime parameters responsible for the phase shift is the value of $\mathrm{d}M_1/\mathrm{d}x$. Calculate this value for an SC(2) 0412 supercritical airfoil around $M = 0.775$ for $c_l = 0.5$ at a Reynolds number of 20 million.

Solution:

A reasonable quick way to investigate the change of Mach number ahead of the shock with the position of the shock is to evaluate the pressure distribution. This has been plotted for three values of the Mach number ($M = 0.77$, $M = 0.775$, and $M = 0.78$) in Fig. 7.41. We see how the small changes in Mach number have a relatively large effect on the shock position. From the jump in pressure coefficient we can calculate the Mach number ahead of the shock wave. First we rewrite the pressure jump in terms of the pressure coefficient using (3.11):

$$\frac{p_2}{p_1} = \frac{\gamma M_\infty^2 C_{p_2} + 2}{\gamma M_\infty^2 C_{p_1} + 2}$$

Furthermore, we rewrite (4.14) to calculate M_1:

$$M_1 = \sqrt{\frac{\gamma + 1}{2\gamma}\left(\frac{p_2}{p_1} - 1\right) + 1}$$

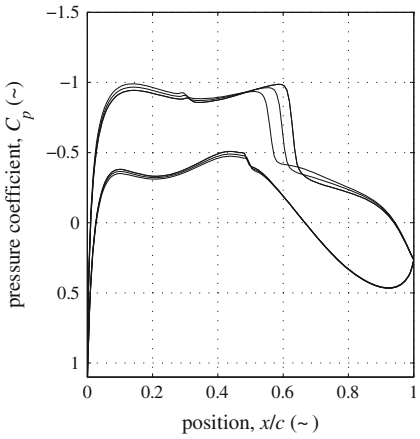

Fig. 7.41 Steady solution for the pressure distribution about an SC(2) 0412 airfoil at $M = 0.77$, $M = 0.775$, and $M = 0.78$

Table 7.1 Change in shock position with Mach number

M	C_{p_1}	C_{p_2}	p_2/p_1	M_1	x_s/c
0.77	−0.935	−0.418	1.35	1.140	0.558
0.775	−0.962	−0.357	1.43	1.169	0.596
0.78	−0.987	−0.299	1.50	1.197	0.627

We tabulate the values for the pressure coefficient, pressure jump, M_1, and the shock position at each Mach number (Table 7.1).

Based on the values of M_1 and x_s/c at the three conditions we make an estimate for $\mathrm{d}M_1/\mathrm{d}x$ according to the following formula:

$$\frac{\mathrm{d}M_1}{\mathrm{d}(x/c)} \approx \frac{1}{2}\left[\frac{1.197-1.169}{0.627-0.596}+\frac{1.169-1.140}{0.596-0.558}\right]=\frac{0.747+0.916}{2}=0.831$$

In the previous example the Mach number in front of the shock wave was still relatively low (≈1.17). Separation would therefore be unlikely. However, the example does demonstrate how one could calculate the change in shock strength with its position. With modern CFD tools unsteady separation from the shock foot can be predicted. In Fig. 7.42 the estimated flow field about a supercritical airfoil is shown at four instances within one oscillation. A numerical approximation of the Unsteady Reynolds-Averaged Navier-Stokes equations is used for these predictions. Errors on the frequency prediction are between 9 and 17 %, which demonstrates that there is still room for improvement. However, the numerical simulations do give us insight into the mechanism of the shock-boundary layer interaction.

The shock motion on the upper surface of the supercritical airfoil of Fig. 7.42 is slightly different from the case of the biconvex circular arc airfoil of Fig. 7.39. In this case, we only have a single shock wave on the upper surface and no shock is formed

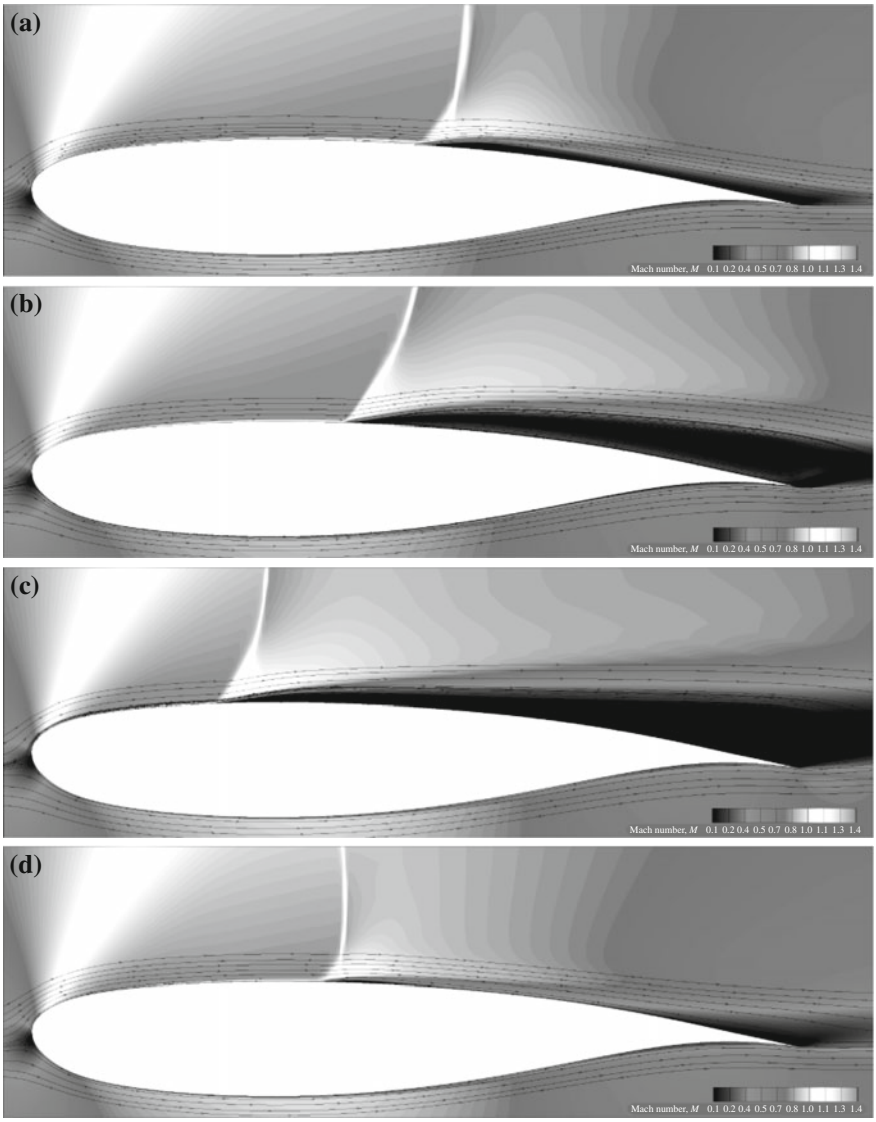

Fig. 7.42 Mach number and flow streamline predictions for the RA16SC1 airfoil at developed buffet conditions, $M_\infty = 0.732$, $\alpha = 4°$, and $\mathrm{Re} = 10^7$ (from Ref. [20]; printed with permission of the authors). **a** Most downstream position of the shock. **b** Middle position as the shock is moving upstream. **c** Most upstream position of the shock. **d** Middle position as the shock is moving downstream

on the lower surface during the cycle. The onset of buffet is shown to start after the onset of flow separation. In other words, the flow has already fully separated from the shock foot and oscillation only starts when the angle of attack is further increased.

As the separated region grows, this high-pressure bubble pushes the shock upstream. When the shock moves upstream it becomes stronger due to a combination of effects. We have discussed the effect of a moving shock on the incident Mach number above. Iovnovich and Raveh [20] call this the *dynamic effect*. In addition, they mention the *wedge effect*, which alludes to the shock becoming more oblique due to the formation of a wedge-like separation region at its foot. The shock strengthens as it moves forward as is evidenced by the increase in inclination angle (Fig. 7.42b). Finally, as the shock moves upstream and encounters more curvature (closer to the leading edge) the region of expansion reduces and the shock strength weakens. In [20] this is referred to as the *curvature effect*. In this example, the boundary layer does not fully reattach at its most forward position (see Fig. 7.42c). Because the Kutta condition is not satisfied, the circulation around the airfoil decreases substantially leading to lower accelerations ahead of the shock. This is another contribution to further weakening of the shock wave. When the flow reattaches the shock moves downstream until separation starts again and the cycle is repeated.

7.7 Summary

In the quest for higher speeds in the late 1940s and early 1950s the wing aerodynamics proved to be the limiting factor. The increase in wave drag that they produced at Mach numbers close to the speed of sound proved to be prohibitive to achieve the desired top speeds. This sparked research into new airfoil shapes that would yield a comparatively low drag coefficient at the specified lift coefficient and Mach number. Originally, laminar-flow airfoils were proposed for this purpose. Their favorable pressure gradient over the first half of the airfoil allowed for a laminar boundary layer up to 50 or 60 % of the airfoil upper surface. Even though these airfoils proved to be suited for subsonic application, they developed strong shock waves at relatively low Mach numbers resulting in excessive wave drag. New airfoils were developed that could decelerate the flow over the upper surface without producing a strong shock. The supercritical airfoil was born.

Shock-free supercritical airfoils are designed to isentropically decelerate the supersonic flow on the upper surface of the airfoil to subsonic conditions. The local Mach number on the upper surface is dominated by the interaction of compression and expansion waves. This interaction is highly dependent on the shape of the sonic line separating the supersonic bubble from the subsonic outer flow as well as on the leading edge radius and the upper surface curvature of the airfoil. A slight change in either of these parameters can cause the compression waves to coalesce and form a shock wave. To avoid this sensitivity, many supercritical airfoils are designed to allow for a (weak) shock wave to terminate the supersonic bubble. The pressure distribution about these airfoils are characterized by a flat plateau over the first half of the airfoil, followed by a sharp drop (normal shock) and a steep adverse pressure gradient towards the trailing edge. The lower surface often has increased camber

near the trailing edge. This increases the pressure on the aft part of the lower surface contributing to a higher lift coefficient for a given angle of attack. A cusped trailing edge is often used to allow for off-surface pressure recovery and a reduction of the adverse pressure gradient preventing trailing-edge stall. In addition, a finite trailing edge thickness has been demonstrated to have a similar effect. Both measures contribute to lower profile drag at the design condition of the airfoil.

The stall of airfoils starts with the separation of the boundary layer. In low speed conditions it has been shown that a limiting Mach number of 1.58 exists on the top surface of the airfoil that effectively "chokes" the flow over continuously convex profiles in conditions where $M_\infty < 1$. This effectively limits the maximum lift coefficient that can be achieved by profiles in subsonic conditions. This Mach number limit is extended to flows over multi-element airfoils (employing flaps and slats). The limiting Mach number can reduce the achievable lift coefficient at Mach numbers as low as 0.25. In addition, a theoretical maximum Mach number of 1.48 exists in front of a normal shock wave. At this Mach number the highest static pressure behind the shock can be achieved for given stagnation conditions. Boundary layer separation is likely to occur at values somewhat below this Mach number. The relatively strong shock causes the boundary layer to separate at its foot. If the resulting separation bubble merges with the separated boundary layer from the trailing edge we have high-speed stall. The interaction between separated boundary layer and shock wave can cause shock oscillation. The resulting high-frequency fluctuation in pressure distribution causes vibrations. These vibrations are referred to as transonic buffet. The buffet boundary forms a limiting line in the Mach-C_L space of a wing that effectively limits the achievable lift coefficient at a specified Mach number.

Problems

Supercritical Airfoils

7.1 Calculate the increase in drag divergence Mach number when we reduce a 10 % thick supercritical airfoil down to 8 % for the same lift coefficient of $c_l = 0.5$.

7.2 Explain why introducing aft-loading on an airfoil can reduce the required supervelocities on the upper surface of the airfoil for a given lift coefficient.

7.3 In graph below the relationship between the drag coefficient and the Mach number of two aircraft are shown: the DC-10-30, and the MD-11, which was the successor of the DC-10. For each lift coefficient the graphs for both aircraft display an exponential increase at the so-called drag-divergence Mach number. Although the drag divergence Mach numbers are similar for both aircraft, the DC-10 suffers from drag creep (a steady increase of the drag coefficient with Mach number) while the MD-11 does not.

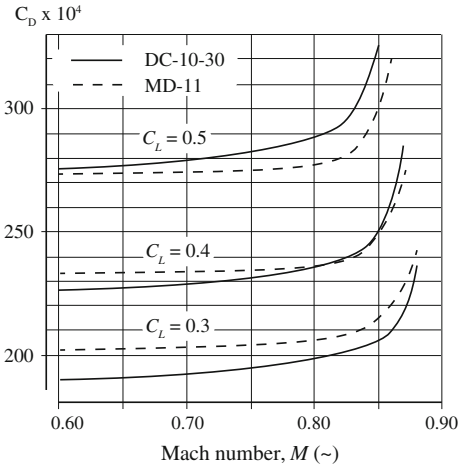

Modified from Ref.[33]

(a) Explain the aerodynamic cause for drag divergence.
(b) Explain the aerodynamic cause for drag creep.
(c) Explain how the addition of aft loading on the MD-11 (the DC-10 did not have any) resulted in less drag for a lift coefficient of 0.5.

7.4 (a) What are the differences between a modern supercritical airfoil and a so-called "sonic rooftop" profile in an aerodynamic sense? Refer in your answer to the critical pressure coefficient.
(b) Indicate the differences in a sketch, drawing the two profiles on top of each other.

7.5 Below the first supercritical airfoil with slot is shown (from Ref. [47]). Can you explain why the addition of a slot resulted in an increase in the drag-rise Mach number?

7.6 Thin trailing edges require a heavier rib structure to be properly supported. Argue why such an increase in structural weight can eventually lead to an increment in (induced) drag.

7.7 The lower rear surface of the wing of the Airbus A340 exhibits a strong camber (see figure below). What are its specific advantages and disadvantages?

Photo R.Slingerland

7.8 The Lockheed P-38 Lightning (below) was in many ways innovative. An unfavorable characteristic was that in straight high-speed dives the aircraft experienced a nose-down pitching tendency (termed *tuck-under* or *Mach tuck*) above $M = 0.65$. This tendency increased the dive angle and thereby the speed even more, leading to structural break-up of the aircraft. Only after the addition of dive recovery flaps this problem was solved. Explain why the nose had the tendency to drop at these Mach numbers.

Photo USAF

Low-Speed Stall

7.9 Show that the Mayer limitation on the minimum pressure distribution corresponds to a static pressure ratio of $p_{\min}/p_\infty \approx 0.30$.

7.10 Consider an airplane with a 1-g stall speed of 66 m/s at 0 m ISA conditions. This stall speed is achieved by deploying slats and flaps. Assume that the suction peak over the slat amounts to $C_p = -24$.

(a) Calculate the stall Mach number at 0 m ISA conditions.
(b) Calculate the minimum allowed pressure coefficient at 0 m ISA using (7.7).
(c) Calculate the stall speed at 1,655 m and Mach number at 1,655 m altitude. Assume the lift coefficient and wing loading are the same at both altitudes.
(d) Calculate the minimum allowed pressure coefficient at 1,655 m altitude.
(e) Based on your calculations, do you think the maximum lift coefficient at 1,655 m is still the same as at sea level?

High-Speed Stall

7.11 Prove that for an airplane in steady, symmetric, and horizontal flight the buffet-onset boundary essentially limits its maximum operational altitude.

7.12 An airplane is cruising at its maximum cruise lift coefficient in steady horizontal flight at a speed of 250 m/s.

(a) Calculate the smallest turn radius it should be able to attain without encountering buffet at $n = 1.3$.
(b) Calculate the associated bank angle to reach $n = 1.3$

7.13 Derive from (7.9) and (4.14) that the pressure jump at which the boundary layer separates at the shock foot amounts to $p_2/p_1 = 1 + \gamma$.

7.14 Consider a shock oscillation on the upper surface of an airfoil. Assume M_1, f, and Δx_0 are as in Example 7.3 and that the chord of the airfoil measures 1m. Furthermore, assume that the static temperature upstream of the shock is constant and amounts to 300 K.

(a) Calculate the phase shift in milliseconds between the shock position, x_s and the pressure jump p_2/p_1 for the following cases:

- $\mathrm{d}M_1/\mathrm{d}x = 5$ (1/m)
- $\mathrm{d}M_1/\mathrm{d}x = 2$ (1/m)
- $\mathrm{d}M_1/\mathrm{d}x = 0.5$ (1/m)
- $\mathrm{d}M_1/\mathrm{d}x = 0$ (1/m)

(b) Calculate the corresponding amplitude of the pressure jump in each of the above cases.
(c) Plot the phase shift *in radians* and the amplitude as a function of $\mathrm{d}M_1/\mathrm{d}x$.

7.15 Consider a shock oscillation on the upper surface of an airfoil. Assume $M_1 = 1.18$, $\mathrm{d}M_1/\mathrm{d}x = 1.5$, and $c = 1$ m. Furthermore, assume that the static temperature upstream of the shock is constant and amounts to 300 K. The amplitude of the shock

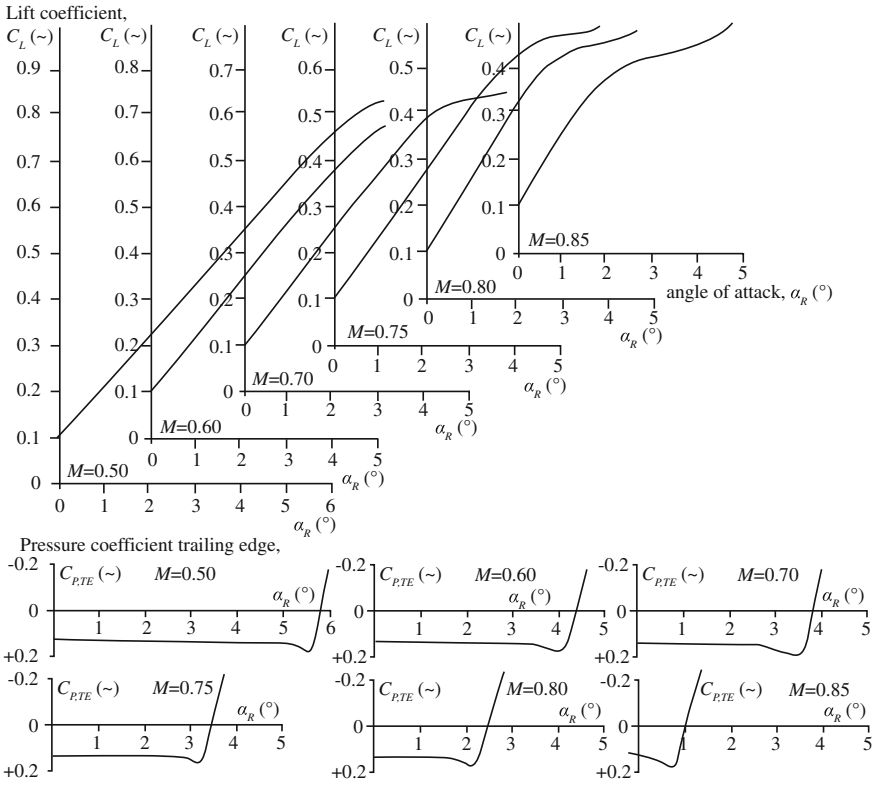

Fig. 7.43 Figure belonging to Problem 7.16

is measured for four frequencies: $f = 10$, 30, 60, and 80 Hz. The corresponding amplitudes measure $\Delta x_0 = 0.105$, 0.102, 0.063, and 0.056, respectively.[8]

(a) Calculate the phase shift in degrees between the shock position, x_s and the pressure jump p_2/p_1
(b) Calculate the corresponding amplitude of the static pressure jump in each of the above cases.
(c) Plot the phase shift *in radians* and the amplitude as a function of the frequency, f.

7.16 In the graphs of Fig. 7.43 the lift curves and trailing edge pressure coefficients are drawn for the outboard wing of a given swept wing. Determine the buffet onset boundary and plot this in an M versus C_L graph.

[8] The data presented in this problem is based on an experiment described in [43]. In this experiment the shock movement was introduced trough a periodic change in angle of attack around $\alpha = 3.0$ of a NLR 7301 airfoil at $M = 0.70$.

References

1. Abbott, I.H., von Doenhoff, A.E.: Theory of Wing Sections. Dover Publications, New York (1959)
2. Anderson, J.: Modern Compressible Flow with Historic Perspective, 3rd edn. McGraw Hill, New York (2003)
3. Anderson, J.: Fundamentals of Aerodynamics, 5th edn. McGraw Hill, New York (2010)
4. Anon.: The supercritical airfoil. NASA TF-2004-13 DFRC (2004)
5. Axelson, J.A.: Estimation of transonic aircraft aerodynamics to high angles of attack. AIAA paper 75-996, Los Angeles (1975)
6. van den Berg, B.: Reynolds number and Mach number effects on the maximum lift and the stalling characteristics of wings at low speed. NLR TR 69025 U, Amsterdam (1969)
7. Blackerby, W., Johnson, J.: Application of advanced technologies to improve C-141 cruise performance. In: 17th Aerospace Sciences Meeting. AIAA 79-0066, New Orleans (1979)
8. Boerstoel, J.W., Uijlenhoet, R.: Lifting aerofoils with supercritical shockless flow. In: Proceedings of ICAS (1970)
9. Carpentieri, G.: An adjoint-based shape-optimization method for aerodynamic design. Ph.D. thesis, Delft University of Technology (2009)
10. Drela, M., Giles, M.B.: Viscous-inviscid analysis of transonic and low Reynolds number airfoils. AIAA J. **25**(10), 1347–1355 (1987). doi:10.2514/3.9789
11. Emmons, H.W.: The theoretical flow of a frictionless, adiabatic, perfect gas inside of a two-dimensional hyperbolic nozzle. NACA TN 1003 (1946)
12. Fischenberg, D., Jategaonkar, R.V.: Identification of aircraft stall behavior from flight test data. In: RTO SCI Symposium on "System Identification for Integrated Aircraft Development and Flight Testing". RTO MP-11, Madrid, Spain (1998)
13. Flaig, A., Hilbig, R.: High-lift design for large civil aircraft. In: AGARD Conference Proceedings CP-515, pp. 31.1–31.12. AGARD (1993)
14. Gibb, J.: The cause and cure of periodic flows at transonic speeds. In: Proceedings of ICAS, pp. 1522–1530. ICAS-88-3.10.1 (1988)
15. Giles, M.B., Drela, M.: Two-dimensional transonic aerodynamic design method. AIAA J. **25**(9), 1199–1206 (1987). doi:10.2514/3.9768
16. Göthert, B.: Widerstandsanstieg bei Profilen im Bereich hoher Unterschallgeschwindigkeiten, Deutche Versuchsanstalt fur Luftfahrt, E.V. Untersuchungen und Mitteilungen Nr. 1167 (1944)
17. Harris, C.D.: NASA supercritical airfoils; a matrix of family related airfoils. NASA TP2969, Langley (1990)
18. Hemenover, A.D.: Tests of the NACA 64-010 and 64A010 airfoil sections at high subsonic Mach numbers. NACA-RM-A9E31. Moffett Field (1949)
19. Hoak, D.E., Anderson, R., Goss, C.R.: USAF Stability and Control Datcom. Air Force Wright Aeronautical Laboratories, Wright Patterson Air Force Base, Ohio (1978)
20. Iovnovich, M., Raveh, D.E.: Reynolds-averaged Navier-Stokes study of the shock-buffet instability mechanism. AIAA J. **50**(4), 880–890 (2012). doi:10.2514/1.J051329
21. Jameson, A., Ou, K.: 50 years of transonic aircraft design. Prog. Aerosp. Sci. **47**(5), 308–318 (2011). doi:10.1016/j.paerosci.2011.01.001
22. Johnson, D.A., Spaid, F.W.: Supercritical airfoil boundary-layer and near-wake measurements. J. Aircr. **20**(4), 298–305 (1983)
23. Kacprznski, J., Ohman, L.H., Garabedian, P.R., Korn, D.G.: Analysis of the Flow Past a Shockless Lifting Airfoil in Design and Off-Design Conditions. NRCC LR-554, Ottawa (1971)
24. Laitone, E.: Local supersonic region on a body moving at subsonic speeds. In: Oswatitish, K. (ed.) Symposium Transsonicum, vol. I, pp. 57–70. Springer, Heidelberg (1964)
25. LeBalleur, J.C., Girodroux-Lavigne, P.: Viscous-inviscid strategy and computation of transonic buffet. In: Zierep, J., Oertel, H. (eds.) Symposium Transsonicum III. IUTAM, pp. 49–63. Springer, Berlin (1988)
26. Lee, B.: Self-sustained shock oscillations on airfoils at transonic speeds. Prog. Aerosp. Sci. **37**(2), 147–196 (2001). doi:10.1016/S0376-0421(01)00003-3

27. Lin, C.C., Rubinov, S.I.: On the flow behind curved shocks. J. Math. Phys. **27**(2), 105–129 (1948)
28. Maki, R., Hunton, L.: Investigation at subsonic speeds of several modifications to the leading-edge region of the NACA 64A010 airfoil section designed to increase maximum lift. NACA TN 3871. Moffett Field (1956)
29. Mayer, J.P.: A limit pressure coefficient and an estimation of limit forces on airfoils at supersonic speeds. NACA RM L8F23, Langley Field (1948)
30. McCullough, G.B., Gault, D.E.: Examples of three representative types of airfoil-section stall at low speed. NACA TN 2502. Moffett Field (1951)
31. McGhee, R., Beasley, W.: Low-speed aerodynamic characteristics of a 17%-thick-airfoil section for general aviation applications. NASA TN-D-7428. Hampton (1973)
32. Nieuwland, G.Y., Spee, B.M.: Transonic airfoils: recent developments in theory, experiment, and design. Annu. Rev. Fluid Mech. **5**, 119–150 (1973)
33. Obert, E.: Aerodynamic Design of Transport Aircraft. IOS Press, Delft (2009)
34. Pearcey, H.H.: Some Effects of Shock-induced Separation of Turbulent Boundary Layers in Transonic Flow Past Aerofoils. National Physics Laboratory R&M 3108 (1955)
35. Pearcey, H.H.: The aerodynamic design of section shapes for swept wings. Adv. Aeronaut. Sci. **3**, 277–322 (1963)
36. Ringleb, F.: Exakte Loesungen der Differntialgleichungen einer adiabatischen Gasstroemung. Zeitschrift fur angewandte Mathematik und Mechanik **20**(4), 185–198 (1940)
37. Roskam, J.: Airplane Design, Part 6: Preliminary Calculation of Aerodynamic, Thrust and Power Characteristics. DARcorp, Lawrence (2006)
38. Smith, A.M.O.: High-lift aerodynamics. J. Aircr. **12**(6), 501–530 (1975)
39. Sobieczky, H., Seebass, A.R.: Supercritical airfoil and wing design. Annu. Rev. Fluid Mech. **16**, 337–363 (1984)
40. Spreiter, J.R., Steffen, P.J.: Effect of Mach and Reynolds numbers on maximum lift coefficient. NACA TN 1044 (1946)
41. Standish, K.J., van Dam, C.P.: Aerodynamic analysis of blunt trailing edge airfoils. J. Sol. Energy Eng. **125**(4), 479 (2003). doi:10.1115/1.1629103
42. Stanewsky, E., Basler, D.: Mechanism and Reynolds Number Dependence of Shock-Induced Buffet on Transonic Airfoils. In: Zierep, J., Oertel, H. (eds.) Symposium Transsonicum III. IUTAM. Springer, Berlin (1988)
43. Tijdeman, H., Seebass, A.R.: Transonic flow past oscillating airfoils. Annu. Rev. Fluid Mech. **12**, 181–222 (1980)
44. Torenbeek, E.: Elements of aerodynamic wing design. Advanced Aircraft Design, Chap. 10. Wiley, Chichester (2013)
45. Viken, J., Wagner, R.D.: Design limits of compressible NLF airfoils. In: 29th Aerospace Sciences Meeting. AIAA-91-0067, Reno (1991). doi:10.2514/6.1991-67
46. Vogelaar, H.: Wind-tunnel investigation on the two-dimensional F-29 model 12-1 airfoil section with various high lift devices at various Mach and Reynolds numbers. NLR TR 83059C (1983)
47. Whitcomb, R.T., Clark, L.R.: An Airfoil Shape for Efficient Flight at Supercritical Mach Numbers. NASA TM X-1109. Langley (1965)